THE UNIVERSITY OF CHICAGO

EFFECTS OF REDSHIFT UNCERTAINTY ON CROSS-CORRELATIONS OF CMB LENSING AND GALAXY SURVEYS

A DISSERTATION SUBMITTED TO
THE FACULTY OF THE DIVISION OF THE PHYSICAL SCIENCES
IN CANDIDACY FOR THE DEGREE OF
DOCTOR OF PHILOSOPHY

DEPARTMENT OF ASTRONOMY AND ASTROPHYSICS

BY

ROSS CAWTHON

CHICAGO, ILLINOIS
AUGUST 2018

Dedicated to my parents, who have always supported me.

"It is the unknown that defines our existence. We are constantly searching, not just for answers to our questions, but for new questions." -Benjamin Sisko

TABLE OF CONTENTS

LIST OF FIGURES

ACKNOWLEDGMENTS

I want to thank Josh Frieman and Scott Dodelson for years of mentorship and help on this work, as well as Steve Kent and Dan Hooper for being on my committee. I also want to thank Sam Passaglia, Chihway Chang, Eric Baxter, Ami Choi, and Ben Hoyle for useful conversations related to this work, and many friends in the Astronomy Department at the University of Chicago for their support. I appreciate the support of the Kavli Institute for Cosmological Physics at the University of Chicago (KICP). My work was specifically supported by KICP through grant NSF PHY-1125897 and an endowment from the Kavli Foundation and its founder Fred Kavli.

ABSTRACT

We explore the effects of incorporating redshift uncertainty into measurements of galaxy clustering and cross-correlations of galaxy positions and CMB lensing maps. We use a simple Gaussian model for a redshift distribution in a redshift bin with two parameters, the mean, z_0 and the width $\sigma_{\rm z}$. We vary these parameters, as well as the galaxy bias, $b_{\rm g}(z)$ and cosmological parameters, $\sigma_8(z)$ and $\Omega_{\rm m}$ in a Fisher analysis across 12 redshift bins from $z = 0 - 7$. We find that incorporating redshift uncertainties degrades constraints on cosmological parameters in the LSST/CMB-S4 era by about a factor of 10. In our fiducial analysis of LSST/CMB-S4, we project constraints on $\sigma_8(z)$ for $z < 3$ of less than 5%. Galaxy imaging surveys are expected to have priors on redshift parameters from photometric redshift algorithms and other methods. When adding priors with the expected precision for LSST redshift algorithms, the constraints on $\sigma_8(z)$ can be improved by a factor of 2-3. We also find that constraints on the redshift parameters from just the galaxy clustering and cross-correlation measurements (with no priors) are competitive compared to photometric redshift techniques. We also project constraints for nearer term survey combinations: DES/SPT-SZ, DES/SPT-3G and LSST/SPT-3G.

CHAPTER 1

INTRODUCTION

Large galaxy imaging surveys provide a wealth of cosmological information about the Universe. In particular, these surveys can probe the growth of structure across cosmic time. Such measurements can distinguish between different models for the mechanism causing cosmic acceleration [28]. Two specific probes used by galaxy surveys to study structure growth are galaxy clustering and weak gravitational lensing. Recent and ongoing imaging surveys using these probes include the Dark Energy Survey (DES, [19]), the Kilo-Degree Survey (KIDS, [15]), the Canada-France-Hawaii Telescope Lensing Survey (CFHTLens, [24]) and the Hyper-Suprime Cam survey (HSC, [38]). The Dark Energy Survey recently produced the most comprehensive study of the growth of structure from an imaging survey [16] using galaxy clustering and weak lensing measurements from its first year of data ([18], [55], [47]). The DES Data Release 1 includes more than 300 million galaxies from the first three years of data ([3]). In the next decade, the constraining power of imaging surveys will increase greatly when the Large Synoptic Survey Telescope (LSST, [35]) begins operations. It is expected to find on the order of several billion galaxies ([29]). LSST will also greatly extend the redshift coverage of imaging surveys.

A special case of using gravitational lensing to infer the structure of matter in the Universe is lensing of the cosmic microwave background (CMB). The CMB is made up of photons that have been free streaming since redshift $z \approx 1100$ (see e.g. [54]). CMB lensing thus measures lensing from matter over nearly the entire lifetime of the Universe, more than 13 billion years. The first detection of CMB lensing was found by doing a cross-correlation of radio galaxies from the NRAO VLA Sky Survey (NVSS) and CMB data from the Wilkinson Microwave Anisotropy Probe (WMAP) ([50]). CMB lensing has since been detected in a number of ways including CMB only methods and cross-correlations with several tracers of large-scale structure, including the cosmic infrared background (CIB), quasars, clusters and galaxies detected in a number of different wavelengths (see [22] for an extensive list).

The cross-correlation of galaxy positions and CMB lensing is a particularly useful measurement of cosmic structure. While CMB lensing maps are impacted by matter back to $z \approx 1100$, they have the disadvantage of having no way to distinguish the redshifts of the matter lensing any particular location in the sky. All the information back to $z \approx 1100$ is stacked into one two-dimensional projection. Galaxies, having redshift measurements, provide a three-dimensional estimate of a location of matter. However, galaxy clustering alone suffers from the fact that galaxies do not directly trace the total underlying distribution of matter in the Universe, but instead are biased tracers. In galaxy clustering measurements, this galaxy bias (the relationship between the distribution of galaxies and total matter) is degenerate with the overall clumpiness of the Universe (i.e. σ_8) which provides information on competing cosmological models. The cross-correlation of galaxies and CMB lensing provides both a measurement of matter as a function of redshift, and breaks the degeneracy of galaxy bias and matter clumpiness. The cross-correlation also has the advantage of having very different systematic effects present. Galaxy surveys (of usually optical or infrared light) and CMB experiments (in the microwave band) operate in a number of different ways, making correlated systematic effects in both surveys unlikely.

These cross-correlations of galaxy clustering and CMB lensing have been measured by a number of recent experiments including the South Pole Telescope (SPT) and Blanco Cosmology Survey galaxies [8], the Planck Satellite and CFHTLens Survey galaxies [43] and both SPT and Planck with Dark Energy Survey galaxies [22]. Recently a projection of the constraining power of a future measurement using LSST and the planned experiment, CMB-S4 [2]) was made by [49]. However, a critical element that many of these studies do not explore in detail is the issue of redshift uncertainties.

While there are spectroscopic galaxy surveys (e.g. BOSS, [14] and in the future, DESI [32]), many of the best cosmological constraints (e.g. [16]) from galaxy clustering and gravitational lensing come from larger, deeper imaging surveys which suffer the downside of having only photometric redshifts from color bands. Much work goes into training these pho-

tometric redshift codes to be as accurate as possible by using spectroscopic training sets of galaxies (e.g. [26], [9] and references therein). Another method of spatially cross-correlating photometric galaxies with smaller samples of spectroscopic galaxies to infer redshift distributions (also known as clustering redshifts) has also seen success (e.g. [39], [11], [13], [21] and references therein). However, even future photometric surveys like LSST expect significant uncertainty in their redshift distributions due to photometric redshift errors. Since LSST will probe higher redshifts than current surveys like the Dark Energy Survey, the issues surrounding photometric redshifts are likely to be compounded. Both the typical photometric training methods and the clustering method need spectroscopic galaxies at the same redshifts probed by the photometric survey. The photometric methods also need spectroscopic samples of galaxies with similar magnitude depth for training. Both getting the necessary number of spectroscopic measurements of galaxy redshifts and insuring that current methods are sufficiently accurate at higher redshifts will be significant challenges.

Another interesting method to infer redshifts that has emerged is the idea of 'self-calibrating' the redshift measurements from cosmological correlation functions themselves (e.g. galaxy clustering, weak lensing measurements etc.) Work by [27] recently explored this idea with several types of correlation functions while holding cosmology fixed. Such methods may be needed in the future to supplement the current methods of photometric redshift calibration.

In this work, we project the constraints of current and future surveys measurements of galaxy clustering and cross-correlations between galaxy positions and CMB lensing. We use a Fisher analysis similar to [49]. Unlike previous work though, we include redshift parameters in the Fisher analysis.

There are two main objectives of this work: 1. To assess how redshift uncertainties affect the expected cosmological constraints from galaxy survey and CMB lensing cross-correlations (i.e. an extension of [49]) and 2. To assess how well the self-calibrating approach can constrain redshift distributions when cosmological parameters are allowed to vary (i.e.

an extension of [27]).

We focus on the cross-correlation of galaxy clustering and CMB lensing to more directly explore these two goals, though we note similar questions could be asked when including optical weak gravitational lensing data which can also be cross-correlated with CMB lensing (see e.g. [5], [31]). For cosmological constraints, we focus on σ_8 as the main parameter that can be studied with these probes. Focusing on this main parameter allows us to study carefully the impact of redshift uncertainties.

The setup of this paper is as follows: In Chapter 2, we discuss the datasets used in this paper and their projected parameters. In Chapter 3 we discuss how we model and parameterize redshift distributions when accounting for photometric redshift errors. In Chapter 4, we outline the projected power spectra measurements used in this work, and the Fisher Matrix formalism we use to project constraints on cosmological and redshift parameters. In Chapter 5, we show Fisher constraints from an analysis without redshift uncertainties. In Chapter 6, we show our fiducial Fisher analysis incorporating redshift uncertainties. In Chapter 7, we explore in more detail how our constraints depend on various survey parameters, including priors on the redshift parameters. In Chapter 8, we explore in more detail how successful our analysis is in constraining the redshift parameters. In Chapter 9, we give our conclusions. In Appendix A, we show the parameter dependence in the power spectra we measure.

CHAPTER 2

DATASETS

2.1 Dark Energy Survey (DES)

The Dark Energy Survey is an ongoing 5-year photometric survey covering 5000 deg^2 in the g, r, i, z, y bands [19]. DES observes from the Blanco Telescope at the Cerro Tololo Inter-American Observatory (CTIO) in Chile. We assume a galaxy distribution for DES from [20] which gives:

$$n(z) \propto (z/z_\star)^\alpha \exp[-(z/z_\star)^\beta] \tag{2.1}$$

where for DES the parameters are $\alpha = 1.25, \beta = 2.29$ and $z_\star = 0.88$ with the total number of galaxies having a density of 12arcmin^{-2}. This redshift distribution is shown in Figure 2.1. This galaxy The full DES will cover 5000 deg^2, however SPT only covers 2500 deg^2, making the observed fraction of the, $f_{sky} = 0.0606$ for the projected power spectra.

2.2 Large Synoptic Survey Telescope (LSST)

The Large Synoptic Survey Telescope is a 10-year photometric survey based at Cerro Pachón in Chile. It is expected to start main operations in 2022. Its main deep-fast-wide survey will cover 18000 deg^2 [29]. For the galaxy distribution in LSST, we match to the prediction used in [49] (Figure 4) for galaxies with i magnitude < 27 after 3 years of data, shown in our Figure 2.1. The prediction comes from LSST simulations in [23] for $0 < z < 4$. We note that for z¡1, this $n(z)$ matches closely the LSST power law prediction from [20]. [49] also add galaxies for $4 < z < 7$ based on recent results from the Subaru Hyper-Suprime Cam GOLDRUSH program [44] which found more than half a million candidates for $4 < z < 7$ galaxies based on the dropout technique ([52]).

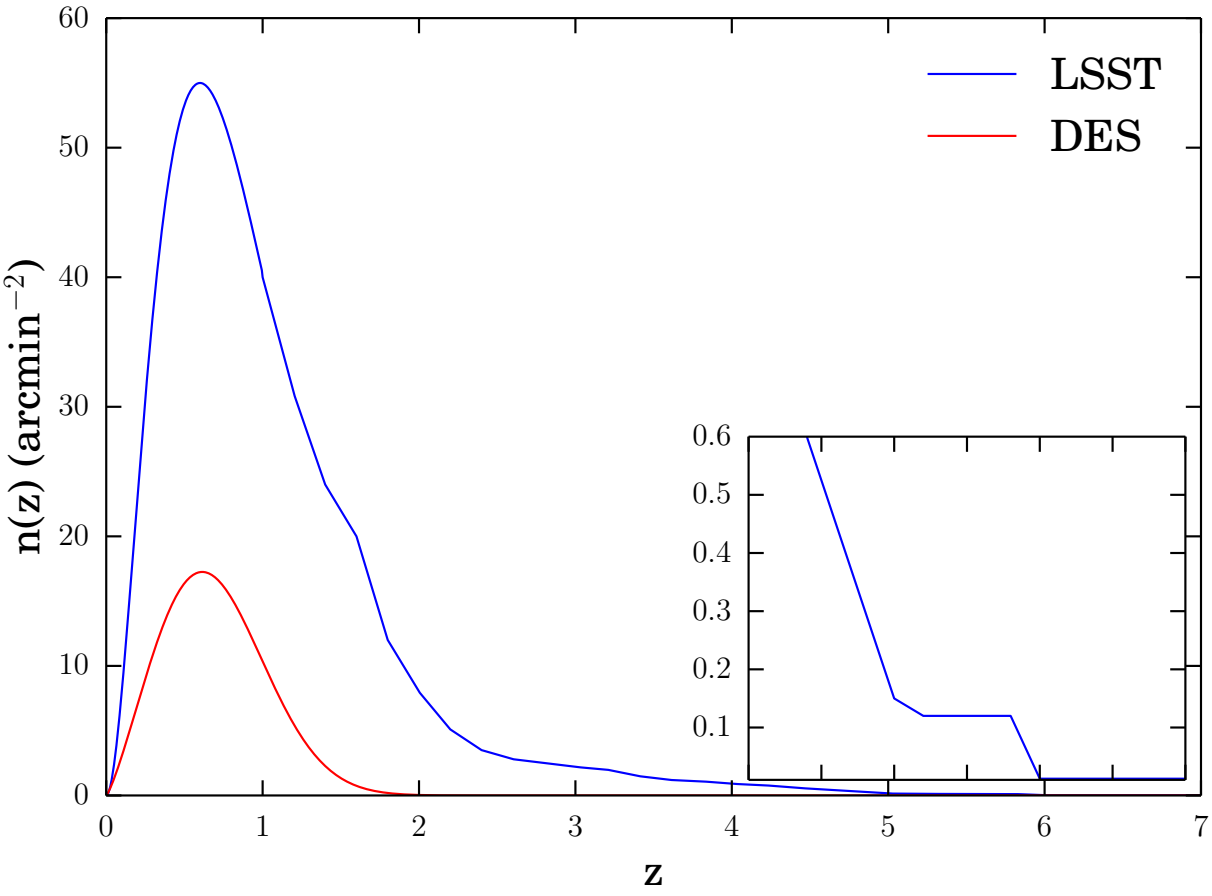

Figure 2.1: The expected galaxy redshift distributions from DES and LSST used in this work. The redshift distributions come from [20] for DES and [49] for LSST. The inset shows $4 < z < 7$.

2.3 South Pole Telescope SZ Survey (SPT-SZ)

The South Pole Telescope (SPT) is a 10-meter millimeter wave, wide-field telescope at the Amundsen-Scott South Pole station in Antarctica [10]. The 2500 deg^2 SPT-SZ survey is described in [53]. A CMB lensing map from this survey was made in [56]. More recently, [42] made a map covering the full survey, while also including data from the Planck Satellite [46]. The lensing maps are made using the quadratic estimator technique [41]. The lensing maps from SPT-SZ are made from measurements in the 150 GHz band. In this band, the temperature maps have a typical noise of $\Delta_T = 18\mu$K arcmin. For the expected CMB lensing noise in the auto-power spectrum (i.e. $N_l^{\kappa\kappa}$), we use the noise measurement in [22] which used a version of the maps made in [56]. The measured lensing noise of the maps in [42] are very similar. The lensing noise for SPT-SZ as well as the projected noise for the following two experiments, SPT-3G and CMB-S4, are shown in Figure 2.2

2.4 South Pole Telescope 3G Survey (SPT-3G)

The SPT-3G survey [7] is the third generation survey on the South Pole Telescope, following the SPT-SZ survey, and the SPT-Pol survey [4]. We will not discuss the SPT-Pol survey due to its smaller sky coverage than SPT-SZ or SPT-3G. SPT-3G has improved pixels and optical design as described in [7]. These improvements should lower the temperature noise by roughly a factor of ten compared to SPT-SZ. Like SPT-Pol, SPT-3G will also have polarization measurements. SPT-3G is expected to produce scientific measurements in the next year or so. It will cover the full 2500 deg^2 which was observed by SPT-SZ. For the projection of SPT-3G noise, we use an estimate by the South Pole Telescope team using a minimum-variance estimator, which is shown in [22]. We show this projected noise in Figure 2.2.

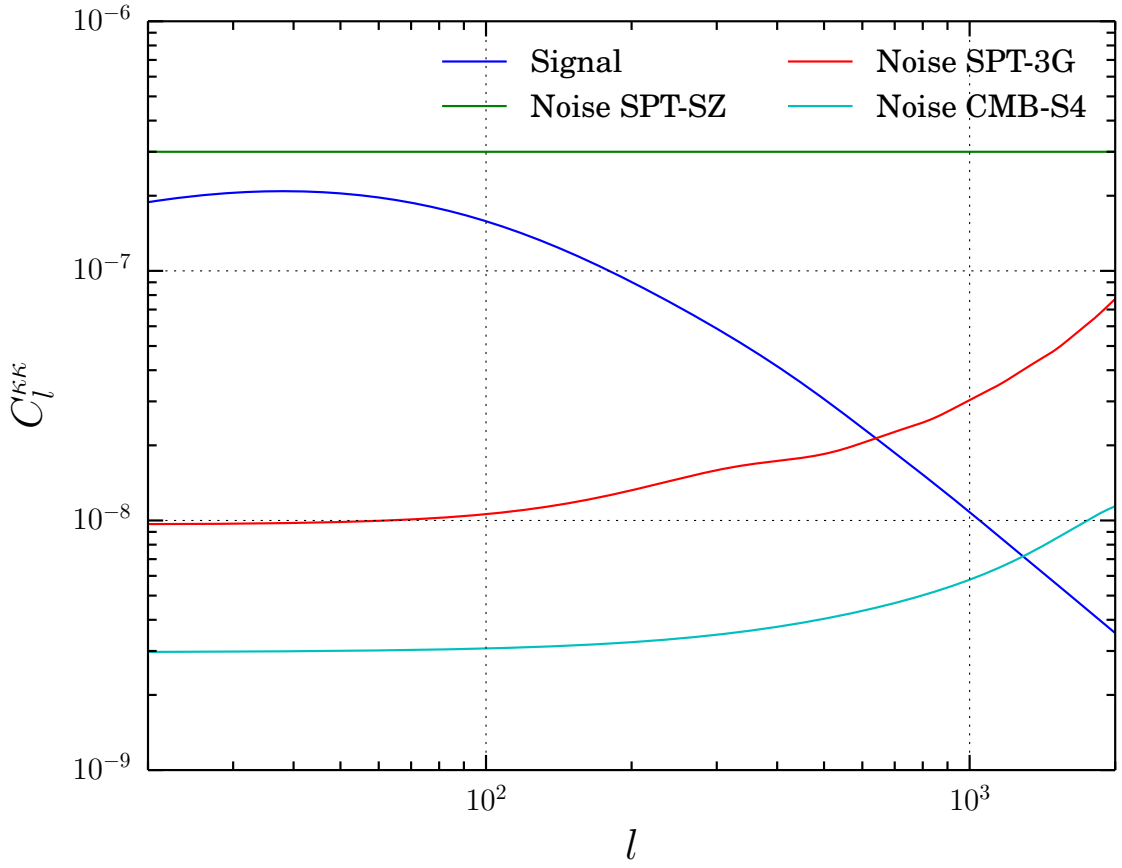

Figure 2.2: The CMB lensing noise for the experiments we consider, as well as the signal of the CMB lensing auto power spectrum, $C_l^{\kappa\kappa}$. We use SPT noise estimates from [22] and the CMB-S4 estimate from [49]. These noise estimates enter our analysis in Equation 4.6.

2.5 Stage 4 Cosmic Microwave Background Experiment (CMB-S4)

The CMB-S4 experiment [1] is a next generation CMB survey expected to begin within the next decade. It is likely to have operations in both Antarctica and Chile. The sky coverage is still uncertain, though many projections have CMB-S4 covering half the sky, overlapping completely LSST. We will assume this for our fiducial analysis, giving $f_{\rm sky} = 0.5$. For the CMB lensing noise, we use the estimate in [49] and show this in Figure 2.2. This estimate assumes $\Delta_T = 1\mu$K arcmin noise and a minimum variance combination of multiple lensing estimators from the T, E and B mode measurements of a CMB experiment [1].

CHAPTER 3

PARAMETERIZING REDSHIFT DISTRIBUTIONS

A focus of this work is to study the effects of redshift uncertainty on cosmological projections using galaxy and CMB lensing surveys. With this in mind, the observed galaxy distributions in a photometric survey like DES or LSST will never quite look like the redshift distributions mentioned in Chapter 2. In a typical photometric survey, galaxies are binned by photometric redshift. High-density, faint samples of galaxies (such as the predicted distribution of $i < 27$ galaxies in LSST in Figure 2.1) typically have photometric redshift errors consistent with a Gaussian scatter. For example, LSST predicts photometric redshifts with a scatter of $\sigma_{\rm ph} = 0.05(1+z)$ around the true redshift ([37], [29]).

To simulate what a photometrically selected and binned redshift distribution looks like, we first take the expected $n(z)$ from the references in Chapter 2. We then draw galaxies from this distribution and assign them photometric redshifts, assuming the photometric redshift errors follow $\sigma_{\rm ph} = 0.05(1+z)$, with no bias (i.e. $\bar{z}_{\rm true} = \bar{z}_{\rm ph}$). We then simulate what would be done for a real survey and bin the galaxies by $z_{\rm ph}$. As can be seen in Figure 3.1, the true redshift distribution (not the photometric redshift distribution) after binning by photometric redshifts is nearly Gaussian in shape. To further show this, in Figure 3.1, we also plot a Gaussian with the mean redshift and standard deviation of the redshifts in the binned n(z). We emphasize that Figure 3.1 shows only true redshift distributions, and does not mimic what a photometric redshift code would predict, as can be seen that, e.g., the n(z) goes beyond the borders of the redshift bin, $z = 1.0$ and $z = 1.5$ (the Gaussian on the right of the Figure).

In current surveys, photometric binning often produces Gaussian-like true redshift distributions in each bin (e.g. in [16]) similar to Figure 3.1. These true redshift distributions are verified to some degree by testing photometric redshift codes on samples of galaxies with spectroscopic redshifts (e.g. [26]) or using other methods like the cross-correlations of photometric and spectroscopic galaxies to recover the redshift distribution of the photometric

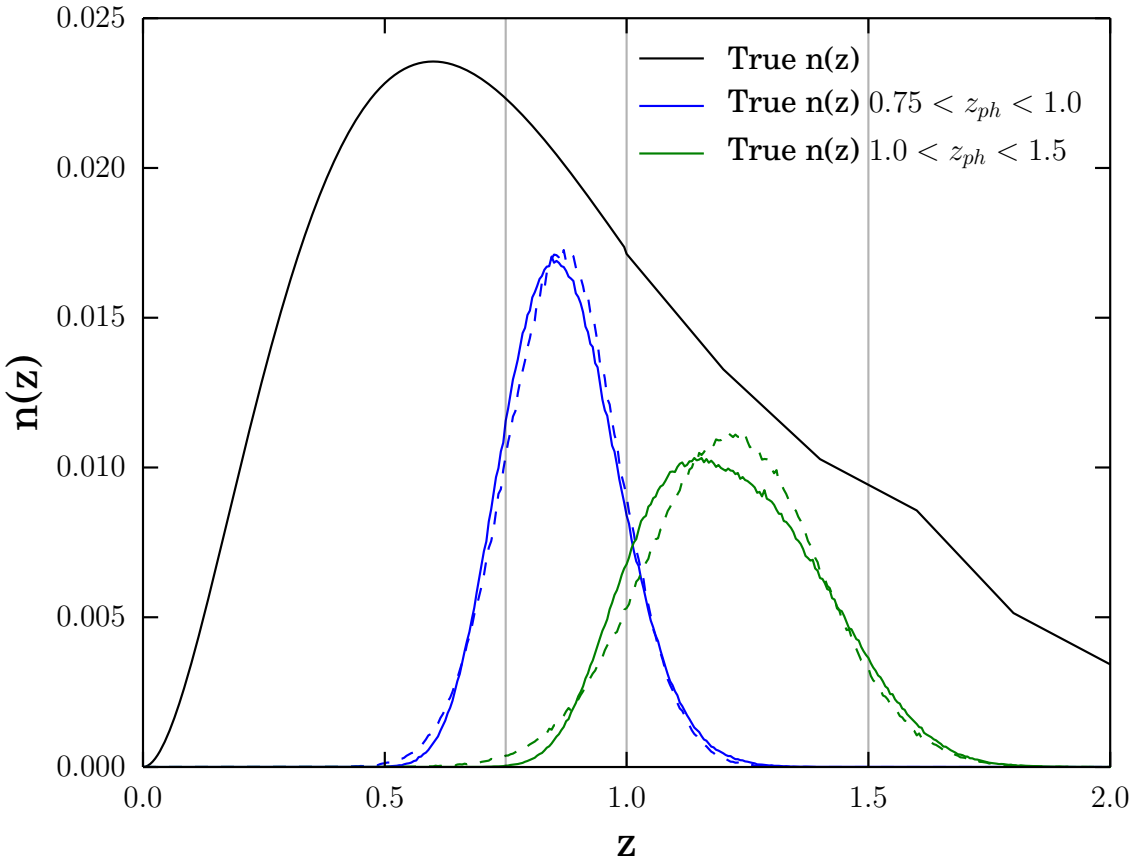

Figure 3.1: The true redshift distribution and examples of photometric redshift bins we use. Shown in black is the true $n(z)$ for LSST, though it actually extends out to $z = 7$. In blue and green are examples of the $n(z)$ in photometrically-selected redshift bins. As seen, e.g. a bin with photometric cutoffs of $z = 0.75$ and $z = 1.0$ (blue) will have its true distribution extend beyond those boundaries. The modeled true distributions of the binned galaxies are close to being Gaussians. The dotted lines show Gaussians with the same mean and standard deviation of the true binned distributions.

set (e.g. [11], [13]). However, each of these methods has uncertainties. Exact knowledge of the redshift distribution for a photometric survey is unlikely.

Given the typical case of a Gaussian-like true redshift distribution when binning by photometric redshifts, we parameterize the redshift distributions in our main analysis (Chapter 6) with Gaussians of mean z_0 and width σ_z. This makes the redshift distribution in a bin, i:

$$n(z)_i \propto \frac{1}{\sigma_{z,i}} \exp[-\frac{(z - z_{0,i})^2}{2\sigma_{z,i}^2}]. \tag{3.1}$$

For our fiducial analysis beginning in Chapter 6, we use 12 tomographic redshift bins with a Gaussian redshift distribution in each bin. These redshift distributions are shown in Figure 3.2, along with the full $n(z)$ prediction for LSST (from [49]). We also show the CMB lensing kernel (described in Equation 4.2) which shows what redshifts most efficiently lens the CMB. The lensing kernel peaks at about $z \approx 2$. In Chapter 6 and later, we allow the parameters $z_{z,i}$ and $\sigma_{z,i}$ of each of the Gaussians in Figure 3.2 to vary in our Fisher analysis (Chapter 4.2). This gives a simple framework for accounting for redshift uncertainties in the Fisher analysis and should be accurate in the limit that the binned redshift distributions are Gaussian.

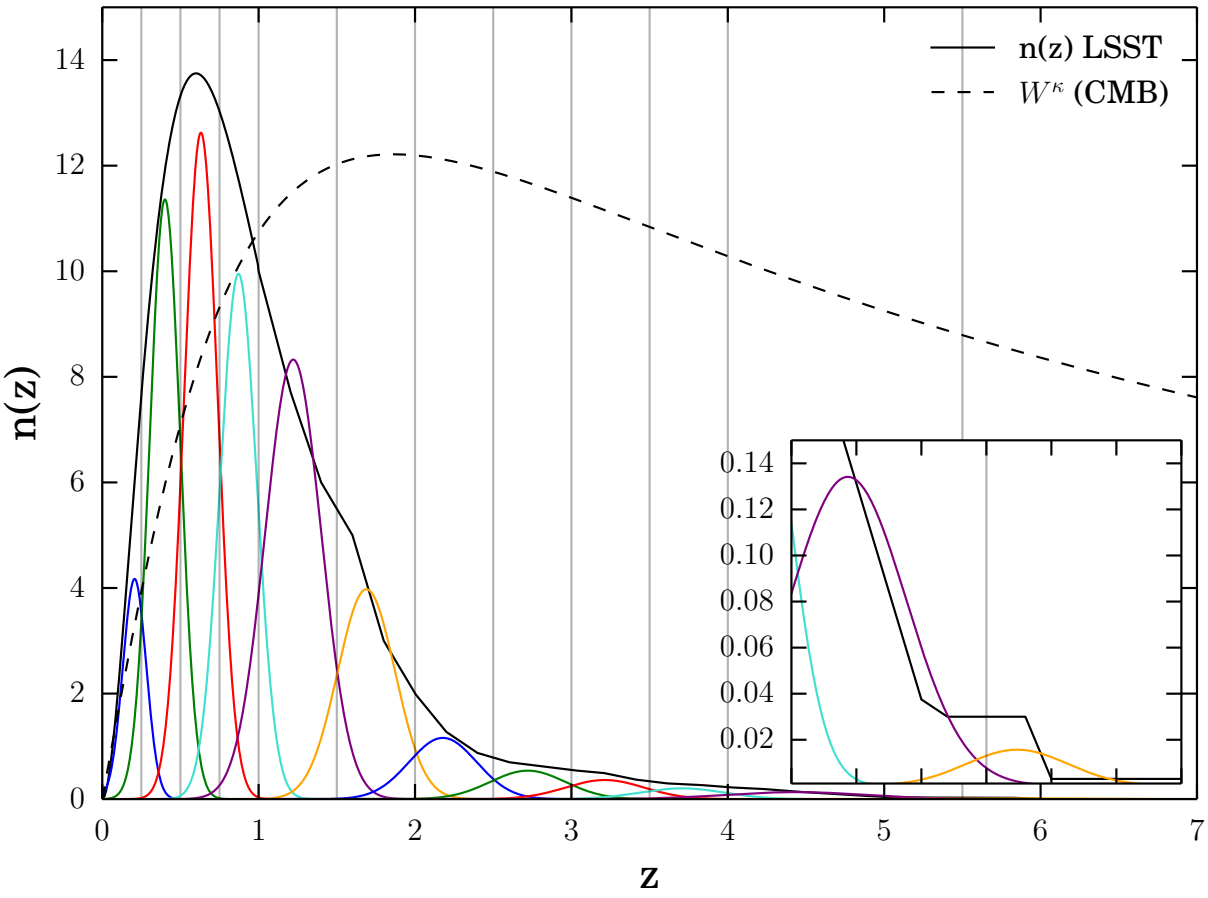

Figure 3.2: The 12 Gaussian redshift distributions for our tomographic redshift bins which will be used in our analysis starting in Chapter 6. Also shown is the full $n(z)$ prediction for LSST, from which the Gaussian distributions are estimated in the manner described in Chapter 3 and Figure 3.1. We also show W^κ from Equation 4.2, which is the CMB lensing kernel. This parameter weights the redshifts that most efficiently lens the CMB. The curve for W^κ is normalized to the full $n(z)$ curve.

CHAPTER 4

METHODS

4.1 Power Spectra

The CMB lensing convergence, κ, in a given line of sight, $\hat{n}$, is the integral over all the matter fluctuations that will cause gravitational lensing:

$$\kappa(\hat{n}) = \int dz W^{\kappa}(z)\delta(\chi(z)\hat{n}, z), \tag{4.1}$$

where $\delta(\chi(z)\hat{n}, z)$ is the overdensity of matter at comoving distance, χ and redshift, z. The distance kernel, W^{κ}, is given by

$$W^{\kappa}(z) = \frac{3}{2}\Omega_{\rm m}H_0^2\frac{(1+z)}{H(z)}\frac{\chi(z)}{c}[\frac{\chi(z_{\rm cmb})-\chi(z)}{\chi(z_{\rm cmb})}] \tag{4.2}$$

where $\Omega_{\rm m}$ is the fraction of the matter density today compared to the present critical density of the Universe, H_0 is the Hubble parameter today, $H(z)$ is the Hubble parameter as a function of redshift, c is the speed of light and $\chi_{\rm cmb}$ is the comoving distance to the surface of last scattering where the CMB was emitted ([8]).

As galaxies are expected to be biased tracers of matter fluctuations, the galaxy overdensity in a given line of sight is

$$g(\hat{n}) = \int dz W^{g}(z) b_{\rm g}(z)\delta(\chi(z)\hat{n}, z), \tag{4.3}$$

where $b_{\rm g}(z)$ is the galaxy bias, the ratio of the overdensity of galaxies to the overdensity of matter, assumed here to be independent of scale, and the kernel W^{g} is given by

$$W^{g}(z) = \frac{1}{n_{\rm tot}}\frac{dn(z)}{dz} \tag{4.4}$$

where $n_{\rm tot}$ is the total number of galaxies in the sample and $\frac{dn(z)}{dz}$ is the redshift distribution

of those galaxies.

At small angular scales, we can use the Limber approximation ([34], [30]) to write the cross power spectrum of two of our fields, i and j, where $i, j \in \kappa_{\rm CMB}, g_{z=0-0.25}, g_{z=0.25-0.5}, ...$ at multipole l as

$$C_l^{ij} = \int \frac{dz}{c} \frac{H(z)}{\chi(z)^2} W^i(z) W^j(z) P(k = \frac{l}{\chi(z)}, z) \tag{4.5}$$

where $P(k = \frac{l}{\chi(z)}, z)$ is the matter power spectrum at wavenumber k for a given redshift z. We calculate all of the power spectra using the Planck 2015 flat-ΛCDM cosmological parameters including external data ([45]). These parameters are $h = 0.6774$, $\Omega_{\rm m} = 0.3089$, $\Omega_{\rm b} = 0.04860$, $\tau = 0.066$, $n_{\rm s} = 0.9667$, $A_{\rm s} = 2.1413 \times 10^9$ at a pivot scale of $k = 0.05$ Mpc^{-1}, corresponding to $\sigma_{8,0} = 0.8159$. The matter power spectrum, $P(k, z)$, is calculated using the Boltzmann code in the CAMB program ([25], [33]) with the program Halofit ([51]) to calculate the non-linear regime of clustering.

We show some sample power spectra in Figure 4.1 for two of the twelve redshift bins used in the fiducial analysis (Figure 3.2). Shown are galaxy auto-correlations, cross-correlations between galaxy bins, and cross-correlations between galaxies and CMB lensing. The error bands represent the covariance ($\mathrm{cov}(C_l^{ii}, C_l^{ii})$) estimates of the LSST/CMB-S4 era. Also shown are some of the relevant noise levels (N_l) for the different experiments. We can see that many more of the multipoles of the cross-correlation between galaxies and CMB lensing are signal dominated in the LSST/CMB-S4 era compared to the DES/SPT-SZ era.

4.2 Fisher Matrix

We use a Fisher Matrix formalism similar to [49] (Section VI) to derive constraints on parameters. The Fisher formalism assumes all the cosmological information is contained in the power spectra, which is true in the limit that the fields are Gaussian. In our fiducial analysis (Chapter 6), we have 12 tomographic redshift bins of galaxies (Figure 3.2), and the

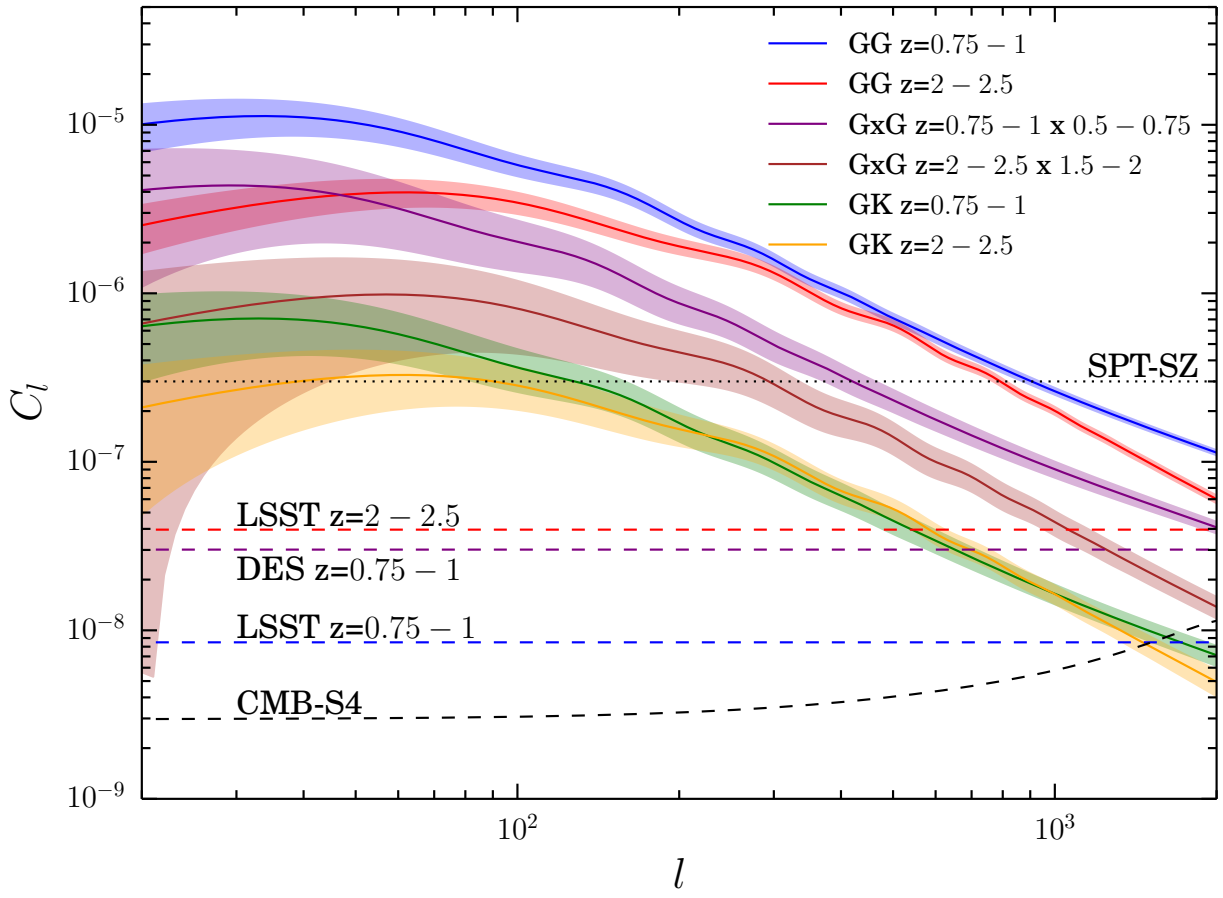

Figure 4.1: Sample angular power spectra (C_l) for different redshift bins (Figure 3.2) in our analysis. Shown are measurements for the bins with photometric redshifts between $z = 0.75 - 1$ and $z = 2 - 2.5$. These measurements include galaxy auto-correlations (GG), cross-correlations between adjacent galaxy redshift bins (GxG) and cross-correlations of galaxies and CMB lensing (GK). Also shown are the noise levels (N_l) for the CMB experiments, SPT-SZ and CMB-S4, and the shot noise for the two galaxy bins in LSST and the $z = 0.75 - 1$ bin in DES.

CMB lensing field, κ. This gives us $N = 13$ fields, which means there are 13 auto-spectra and $N(N-1)/2 = 78$ cross-spectra, for a total of 91 spectra. However, we assume the cross-spectra of non-neighboring redshift bins are zero. This reduces the total number of non-zero spectra to $3(N-1) = 36$.

The Gaussian covariances for the power spectra, C_l are:

$$\mathrm{cov}(\hat{C}_l^{ij}, \hat{C}_l^{i'j'}) = \frac{\delta_{ll'}}{f_{\mathrm{sky}}(2l+1)} + (\hat{C}_l^{ii'}\hat{C}_l^{jj'} + \hat{C}_l^{ij'}\hat{C}_l^{ji'}) \tag{4.6}$$

where the upper indices i and j again refer to the different fields. The power spectra denoted by $\hat{C}$ include noise:

$$\hat{C}_l = C_l(\mathrm{theory}) + N_l \tag{4.7}$$

where for galaxy auto-correlations, the shot noise term is $N_l = 1/\rho$ where ρ is the galaxy density per steradian, and for the CMB lensing auto-correlation, the predicted N_l for different CMB experiments is shown in Figure 2.2. For cross-correlations, $N_l = 0$. Equation 4.6 ignores non-Gaussian corrections for CMB lensing and galaxy clustering covariance.

Again following [49], we define a large one-dimensional vector containing all the spectra:

$$d = (d_{l_{\mathrm{min}}}, d_{l_{\mathrm{min}+1}, ..., d_{l_{\mathrm{max}}}}). \tag{4.8}$$

For each l,

$$d_l = (C_l^{11}, C_l^{12}, ..., C_l^{NN}) \tag{4.9}$$

with N being the number of fields. Since $C_l^{ij} = C_l^{ji}$, d_l has $N(N+1)/2$ spectra, 91 spectra when $N = 13$ fields, with only 36 of these being non-zero as mentioned previously. The Fisher Matrix is then:

$$F_{ab} = \sum_{l=l_{\rm min}}^{l_{\rm max}} \frac{\partial d_l}{\partial \theta_a} [{\rm cov}(d_l, d_l)]^{-1} \frac{\partial d_l}{\partial \theta_b} \tag{4.10}$$

where a, b index the parameters varied. For our fiducial analysis, we use $l_{\rm min} = 20$ and $l_{\rm max} = 1000$, though we test other $l_{\rm max}$ values. In all cases, we do not bin in l in this work. This Fisher setup assumes that the fields overlap (i.e. the CMB and galaxy experiments overlap completely on the sky), which is the case in the projected experiments of Chapter 2. The projected error on a parameter, θ, is then:

$$\sigma(\theta_a) \geq \sqrt{(F^{-1})_{aa}}. \tag{4.11}$$

In Chapter 7.6, we analyze the effects of adding priors to our analysis. We add priors by substituting:

$$F_{aa} \rightarrow F_{aa} + \frac{1}{p(\theta_a)} \tag{4.12}$$

where $p(\theta_a)$ is the prior on the parameter. When applying priors, Equation 4.12 is applied before the Fisher Matrix is inverted in Equation 4.11.

In our fiducial analysis, there are five types of parameters varied. These include the redshift parameters, $z_{0,i}$ and $\sigma_{{\rm z},i}$ defined in Equation 3.1 for each of the redshift bins indexed by i. We also vary for each redshift bin, $b_{{\rm g},i}$, the galaxy bias and $\sigma_{8,i}$, which measures the amplitude of the matter power spectrum on scales of 8 h^{-1} Mpc, where $h = 100$ km/sec/Mpc/H_0. We use parameterizations similar to [49] for both parameters. In Equation 4.3, we model the galaxy bias $b_{{\rm g},i}$ as:

$$b_{{\rm g},i} = B_i(1+z). \tag{4.13}$$

While we will quote results on $b_{{\rm g},i}$ through out this work, effectively the parameters being varied in the Fisher analysis is B_i. We implement $\sigma_{8,i}$ into the power spectra (Equation 4.5)

by substituting:

$$P(k,z) \rightarrow (1+s_i)^2 P(k,z) \tag{4.14}$$

where $s_i \equiv (\sigma_{8,i}/\sigma_{8,\rm fid} - 1)$ is the fractional difference of σ_8 in that bin compared to the fiducial cosmology. We note that when we calculate the CMB lensing auto-correlation,$C_l^{\kappa_{\rm CMB}\kappa_{\rm CMB}}$ we apply s_i from the minimum and maximum photometric redshift boundaries for each bin i, though this does not map perfectly to the redshifts of the galaxies in bin i. [1]

The fifth type of parameter we allow to vary is the matter density of the Universe, $\Omega_{\rm m}$. This parameter enters into $P(k,z)$, the calculation for $H(z)$ as well as in the CMB lensing kernel, $W^{\kappa}(z)$ (Equation 4.2). When we vary $\Omega_{\rm m}$, we also vary Ω_Λ, the cosmological constant energy density in ΛCDM, to keep the Universe flat.

The parameters $z_{0,i}, \sigma_{{\rm z},i}, b_{{\rm g},i}$ and $\sigma_{8,i}$ are measured in each redshift bin. Along with $\Omega_{\rm m}$, this gives a total of n=4(N-1)+1 parameters, which is 49 in the case of N=13 fields. The Fisher matrix will be n x n in size.

1. Since unlike [49], our redshift bins overlap, we must make a choice whether to tie the definition $\sigma_{8,i}$ to a specific redshift range, or to a specific redshift binned sample. We choose the latter as that is how many photometric redshift binned samples are analyzed (e.g. [22]). However, this does make how to specifically calculate $\partial C_l^{\kappa_{\rm CMB}\kappa_{\rm CMB}}/\partial\sigma_{8,i}$ ill defined since we are not defining $\sigma_{8,i}$ to be a precise redshift range. In any case, the contributions of $C_l^{\kappa_{\rm CMB}\kappa_{\rm CMB}}$ are very minor in the analysis, so we do not think this impacts the results significantly.

CHAPTER 5

RESULTS WITH NO REDSHIFT UNCERTAINTY

We first analyze the results of a Fisher matrix analysis when there is no redshift uncertainty. We briefly do an analysis that allows us to compare most directly to the results in [49]. We use the full $n(z)$ of LSST (black line in Figure 3.2) and not the Gaussian redshift distributions as will be used in Chapter 6. We divide this $n(z)$ into the 6 tomographic bins used in [49] with boundaries at $z = [0, 0.5, 1, 2, 3, 4, 7]$. Since there is no redshift uncertainty, here our Fisher setup has 6 values for $\sigma_{8,i}$ and $b_{\mathrm{g},i}$ and Ω_{m} for 13 parameters. [49] do not vary Ω_{m}, so we also show results without this parameter. We show the constraints on σ_8 for this setup in Figure 5.1. We show how the results change as a function of l_{max} in Figure 5.2. These constraints are nearly identical to [49] (Figure 9) when not including Ω_{m} and only marginally larger with Ω_{m}. The largest difference in our analysis here compared to [49] is that we do not include any SDSS or DESI galaxies at low redshifts as they do. This makes their constraints in the two lowest redshift bins better. Since [49] does not vary Ω_{m}, we show results with and without that parameter varying in Figures 5.1-5.2. The errors on σ_8 grow between $30 - 60\%$ when varying Ω_{m}.

For our fiducial analysis in Chapter 6, we will use smaller redshift bins, splitting each of the bins used in [49] in half, giving us the 12 redshift bins shown in Figure 3.2. These smaller redshift bins are more similar to current analyses on data, such as from the Dark Energy Survey (e.g. [22], [16]). The approximation of a Gaussian redshift distribution as a result of photometric redshift binning (Chapter 3) is also more accurate for smaller redshift bins. We first test the effect of the smaller bins while still having no redshift uncertainty. We divide the LSST $n(z)$ distribution directly into twelve tomographic bins with boundaries at $z = [0, 0.25, 0.5, 0.75, 1, 1.5, 2, 2.5, 3, 3.5, 4, 5.5, 7]$. Again, we assume all redshifts can be known directly from the black line in Figure 3.2, and do not use the Gaussian distributions of that figure yet. In this setup, our Fisher analysis has 12 values for $\sigma_{8,i}$ and $b_{\mathrm{g},i}$ and Ω_{m} for 25 parameters. The constraints on σ_8 and b_{g} in this setup are shown in Figure 5.3. We

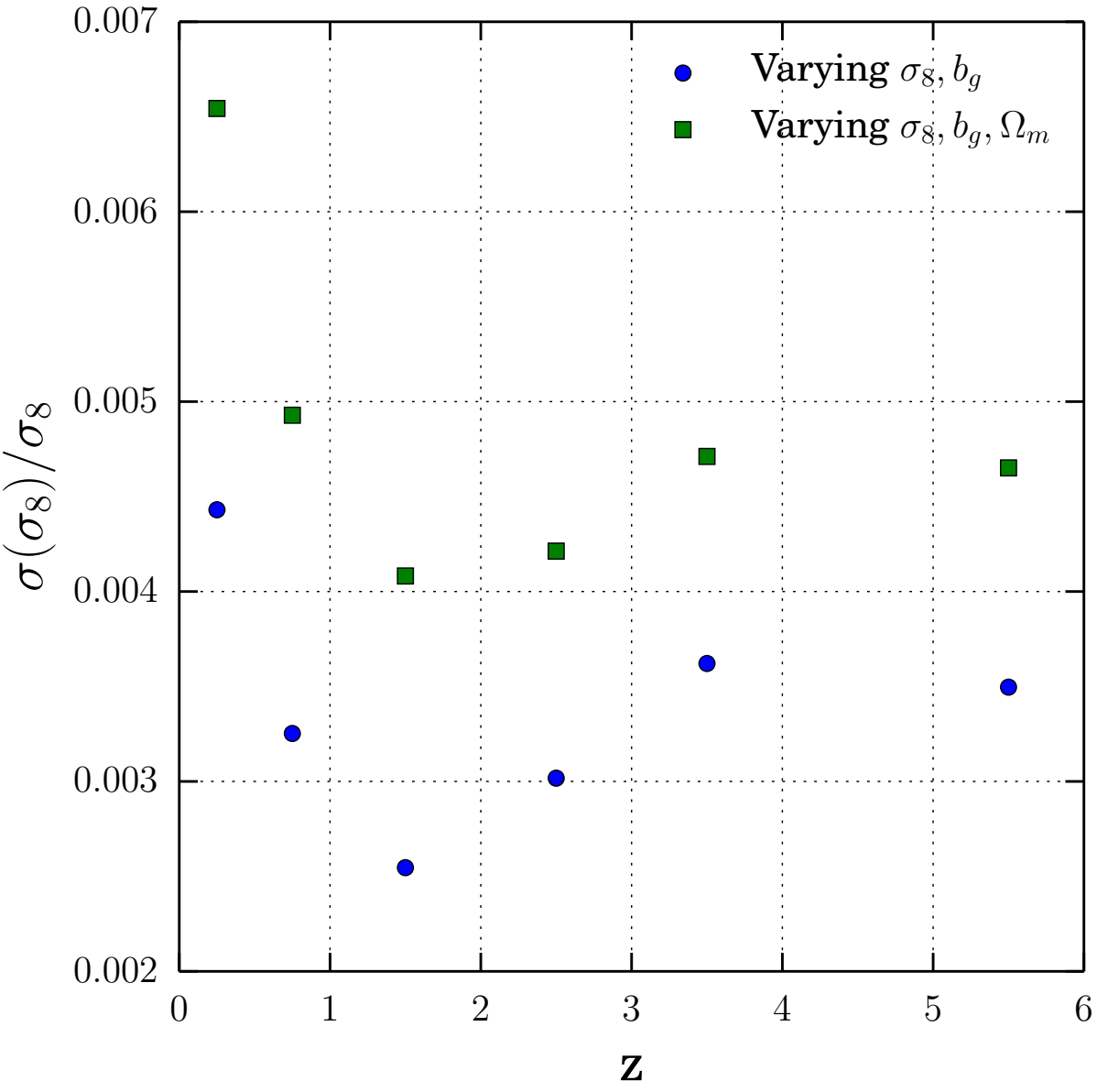

Figure 5.1: The constraints on σ_8 in the scenario with with no redshift uncertainty for the LSST/CMB-S4 era. We plot both the case with σ_8 and b_g allowed to vary in each bin (to be able to compare with the analysis in [49]) as well as the case with also Ω_m being allowed to vary.

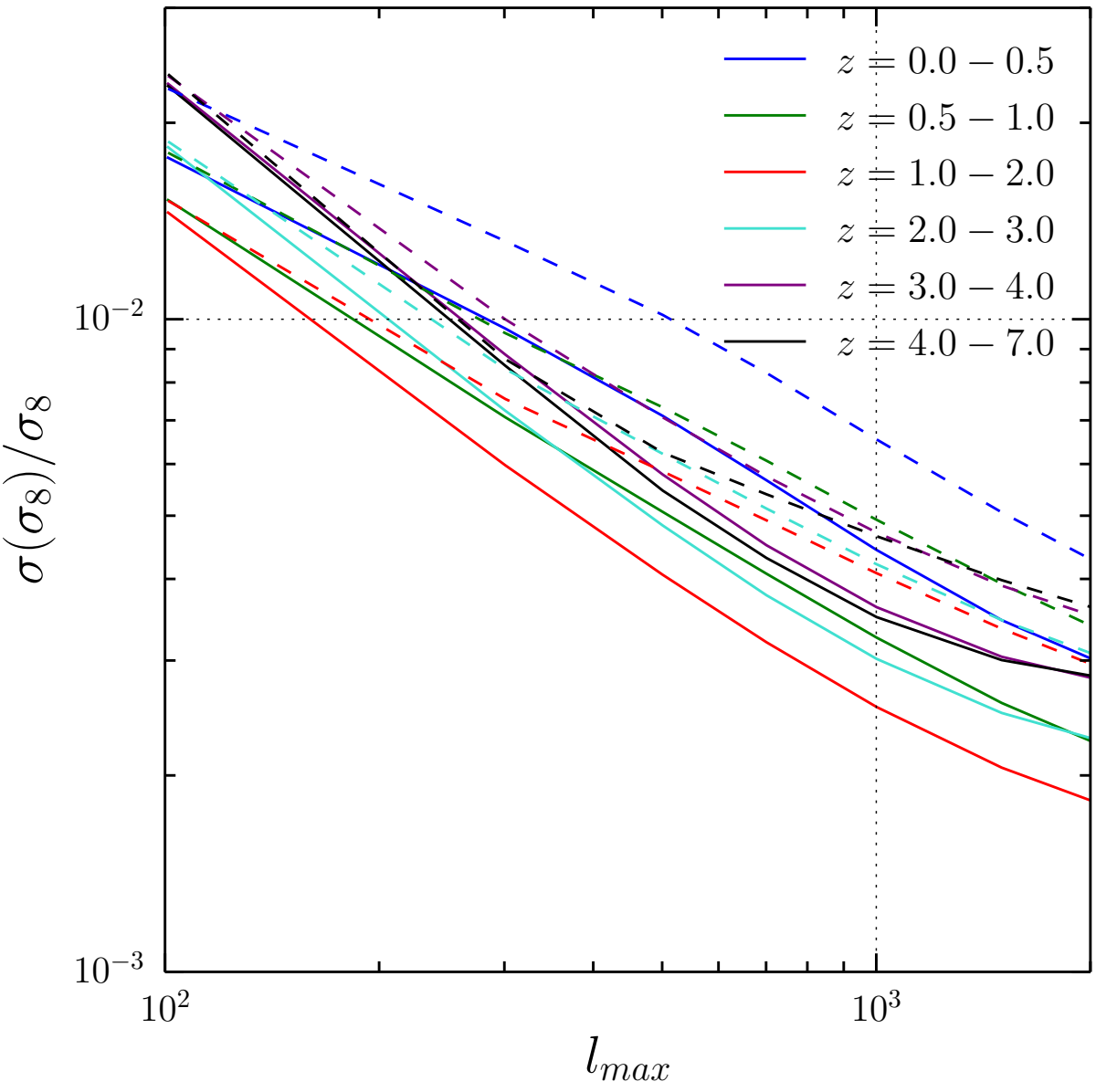

Figure 5.2: Same analysis of σ_8 constraints while having no redshift uncertainty as Figure 5.1, but with varying $l_{\rm max}$ in the LSST/CMB-S4 era. This allows a direct comparison with the analysis of [49] (Figure 9). Our results are very similar. The dotted lines are for the case when we allow $\Omega_{\rm m}$ to vary as well, while the solid lines are with only varying σ_8 and $b_{\rm g}$.

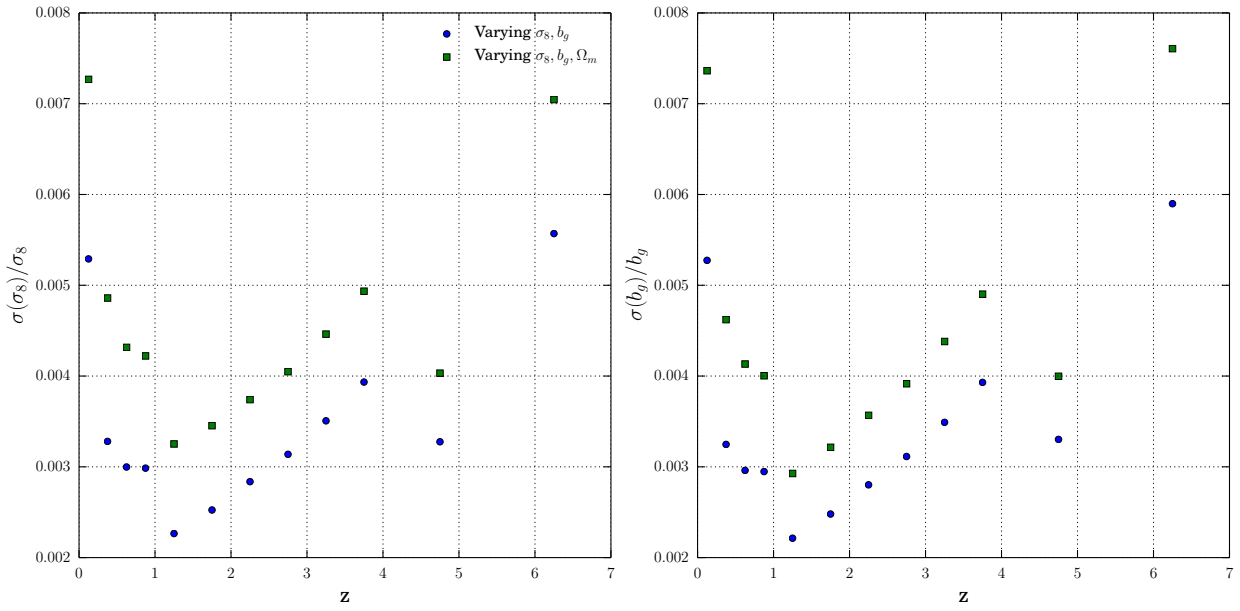

Figure 5.3: Fractional constraints on σ_8 and b_g as a function of redshift for the case of 12 tomographic redshift bins, and no redshift uncertainty. Plotted are the cases where Ω_m is fixed or allowed to vary. The constraints largely weaken with higher redshift as the number density drops, however at $z = 1.25$ and $z = 4.75$, the redshift width of the bin increases, leading to larger numbers of galaxies in the bin and smaller constraints.

again show the case with and without Ω_m in the figures as well. Compared to Figure 5.1, the constraints on σ_8 from doubling the number of redshift bins when not using Ω_m are a little worse, as expected from shrinking the number of galaxies in each bin. The constraints are about $25 - 50\%$ larger when comparing the average of two smaller bins with the larger bin of the same redshift range (e.g. comparing the average constraint between of $z = 0 - 0.25$ and $z = 0.25 - 0.5$ to the constraint on $z = 0 - 0.5$). Of course, the benefit of more bins is gaining more precise information of the full $\sigma_8(z)$. Interestingly, when also varying Ω_m, the constraints on σ_8 have very little degradation when switching from 6 bins to 12 bins. With Ω_m varying, the constraints on the smaller bins approximately equal the constraints on the larger bins (Figures 5.1 and 5.3). This is explained by the greater constraints on Ω_m when increasing the number of bins (and thus, measurements to infer Ω_m). The constraints go from $\sigma(\Omega_m) = 0.0007$ with 12 bins to $\sigma(\Omega_m) = 0.0003$ with 6 bins.

CHAPTER 6

RESULTS WITH REDSHIFT UNCERTAINTY

In this section, we show the fiducial analysis of varying five parameters in the Fisher analysis of Chapter 4.2: $\sigma_8(z)$,$b_{\rm g}(z)$,$z_0(z)$,$\sigma_{\rm z}(z)$ in each redshift bin, and $\Omega_{\rm m}$. With 12 redshift bins for our main analysis of an LSST-like sample, we have 49 parameters. The redshift distributions with central values of $z_0(z)$ and Gaussian width $\sigma_{\rm z}(z)$ are shown in Figure 3.2.

For our fiducial analysis of the LSST/CMB-S4 era including redshift uncertainties, we show our constraints on the the various parameters in Figures 6.1-6.2. Figure 6.1 shows the constraints on $\sigma_8(z)$, and $b_{\rm g}(z)$, in the cases with and without redshift uncertainty (i.e. with $z_0(z)$ and $\sigma_{\rm z}(z)$ fixed.) We can see that the addition of redshift uncertainty in these parameters increases errors on the other parameters by roughly a factor of ten. We also show the results for the parameters when cross-correlations of galaxy bins are not used. In this case, errors on parameters tend to increase by a factor of two or more. This highlights the importance of the cross-correlations between galaxy bins, a measurement that in principle is not necessary when galaxy redshifts are known perfectly, and galaxy bins do not overlap in redshift space.

Figure 6.2 shows the constraints on the redshift parameters z_0 and $\sigma_{\rm z}$ in each of the 12 photometric bins. We again also plot the results when not using the galaxy-galaxy cross-correlations of adjacent redshift bins (labeled as 'no GxG'). As seen in the figure, the galaxy cross-correlations are of particular importance for $\sigma_{\rm z}$. The cross-correlations break degeneracies between σ_8, $b_{\rm g}$ and $\sigma_{\rm z}$ that remain when only having galaxy auto-correlations and galaxy-CMB lensing cross-correlations for each bin (see Appendix A for more discussion).

We also note that the constraints on $\Omega_{\rm m}$ in the scenarios of no galaxy cross-correlations, the fiducial analysis, and the no redshift uncertainty case are $\sigma(\Omega_{\rm m}) = [0.00075, 0.00060, 0.00025]$ respectively. The improvement on $\Omega_{\rm m}$ with more redshift information is more mild than on σ_8 due to $\Omega_{\rm m}$ not being part of the degeneracy of σ_8, $b_{\rm g}$ and $\sigma_{\rm z}$ (Appendix A).

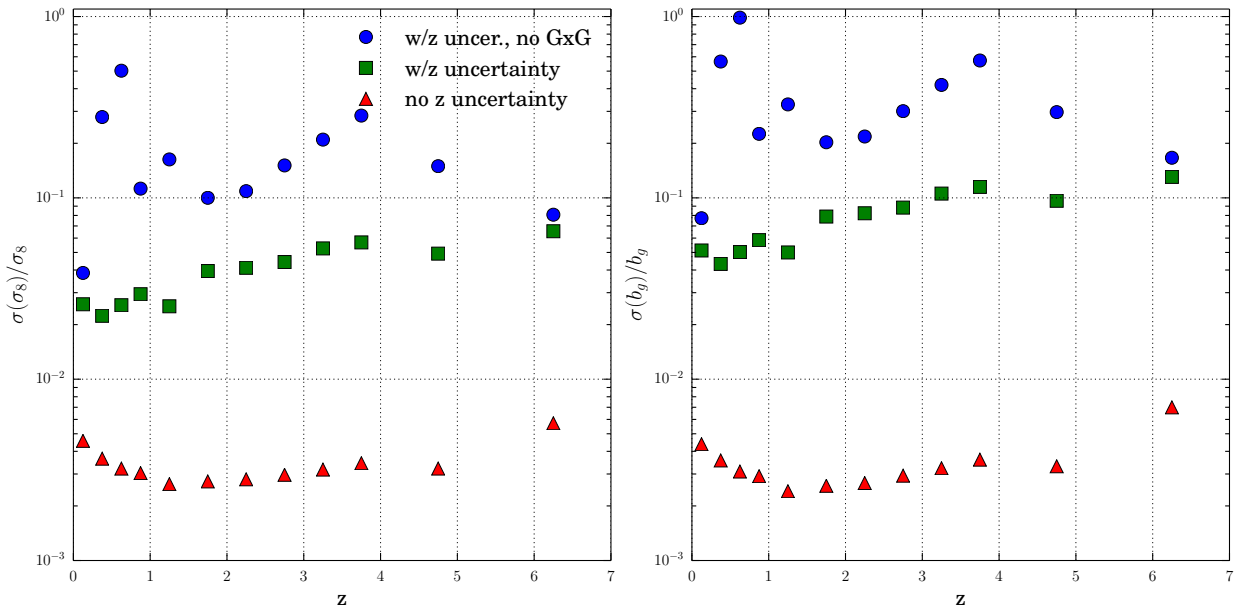

Figure 6.1: Fractional constraints on σ_8 and b_g for the fiducial case of LSST+CMB-S4, with $l_{\rm max} = 1000$, and $f_{\rm sky} = 0.5$. Shown are the results with no redshift uncertainty, varying $b_{{\rm g},i}$, $\sigma_{8,i}$ for each redshift bin, as well as $\Omega_{\rm m}$. Also shown is the main analysis where we include redshift uncertainty by allowing the parameters $z_{0,i}$ and $\sigma_{{\rm z},i}$ to vary in each bin. We also show the case where we have redshift uncertainties, but do not use the cross-correlations of two adjacent galaxy bins in redshift space ('no GxG').

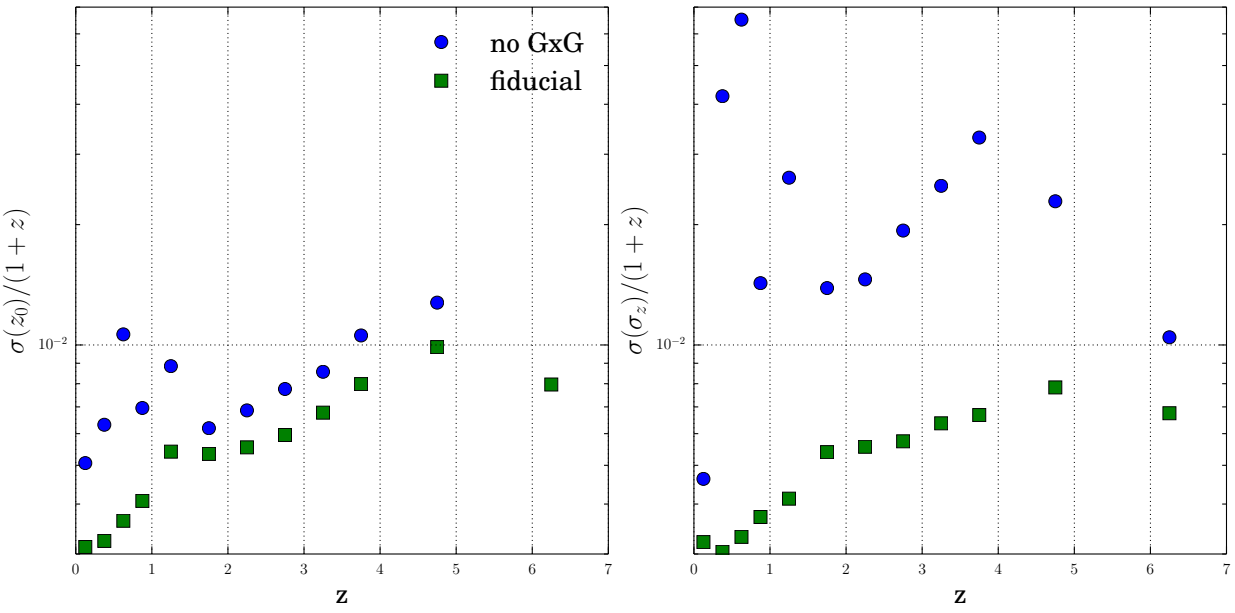

Figure 6.2: The constraints on the mean redshift, z_0, and the width of the redshift distribution, σ_z, in each redshift bin for our fiducial analysis of Figure 6.1. We also show the constraints when the cross-correlations of two adjacent galaxy bins in redshift space are not used ('no GxG').

CHAPTER 7

DEPENDENCE ON SURVEY PARAMETERS

7.1 Example: DES-SPT

In this section, we vary different survey parameters that affect the precision of the constraints on the five types of parameters. We first look at a specific example of varying the survey parameters, using the expected galaxy density and redshift distributions from the full Dark Energy Survey, and CMB lensing noise from SPT-SZ and the future SPT-3G. This represents a nearer term projection for parameters using our methodology.

Figure 7.1 shows the constraints for the four parameters that exist in each redshift bin for DES+SPT-SZ, LSST+SPT-3G and our fiducial analysis on LSST+CMB-S4. Not shown are the constraints for the combination of DES+SPT-3g. These constraints are within 5% of the constraints for LSST+SPT-3G, in the bins where DES has data (the first 5 data points, up to $z < 1.5$), so we do not show them. While the DES/SPT-SZ constraints are approximately factors of 2-3 weaker than LSST/CMB-S4, a $\approx 10\%$ constraint on σ_8 is still possible in all of our bins, and should be achievable with these surveys in the next few years. We show the constraints on $\Omega_{\rm m}$ for the different era analyses in Figure 7.2. We see that the constraints on $\Omega_{\rm mm}$ improve by a factor of about 3-5 from the SPT/SZ era to the LSST/CMB-S4 era. We also see that all eras of measuring the power spectra used in this work should improve upon the constraints from the recent DES year 1 analysis of galaxy clustering and weak lensing plus other data sets [16].

7.2 Dependence on $l_{\rm max}$

The largest multipole, $l_{\rm max}$ (smallest scale) to which these measurements can be used and modeled for is a parameter with still a fair bit of uncertainty. In [22], $l_{\rm max} = 2000$ was used for correlations of DES science verification data and SPT-SZ. However, in [6], they realize

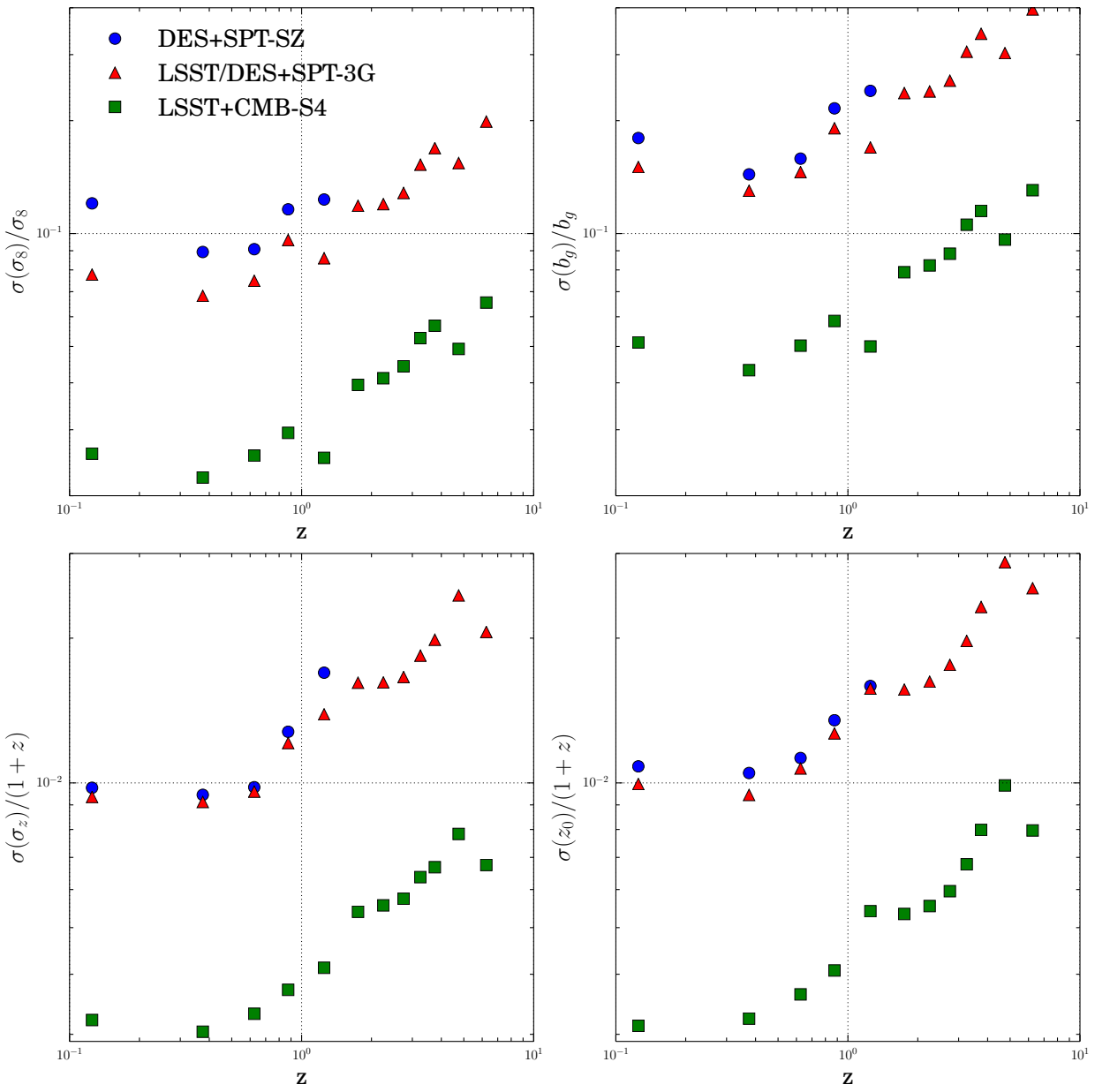

Figure 7.1: The Constraints on all four of our redshift bin parameters, σ_8, b_g, z_0 and σ_z for each of the survey combinations for our fiducial analysis including redshift uncertainties. Each of the surveys use $l_{\rm max} = 1000$. The correlations with SPT have $f_{\rm sky} = 0.061$ (2500 deg^2) and the correlation of LSST and CMB-S4 has $f_{\rm sky} = 0.5$ (20000 deg^2). The results for DES+SPT-3G and LSST+SPT-3G are within 3% of each other for the redshift bins DES goes up to, so only LSST+SPT-3G is plotted. In general constraints are better with higher densities and thus decrease with redshift, though there are exceptions where the binsize is increased (e.g. $z = 1.25$). We plot here logarithmically on the x-axis to give more space in showing the DES constraints while still showing the full redshift range of LSST.

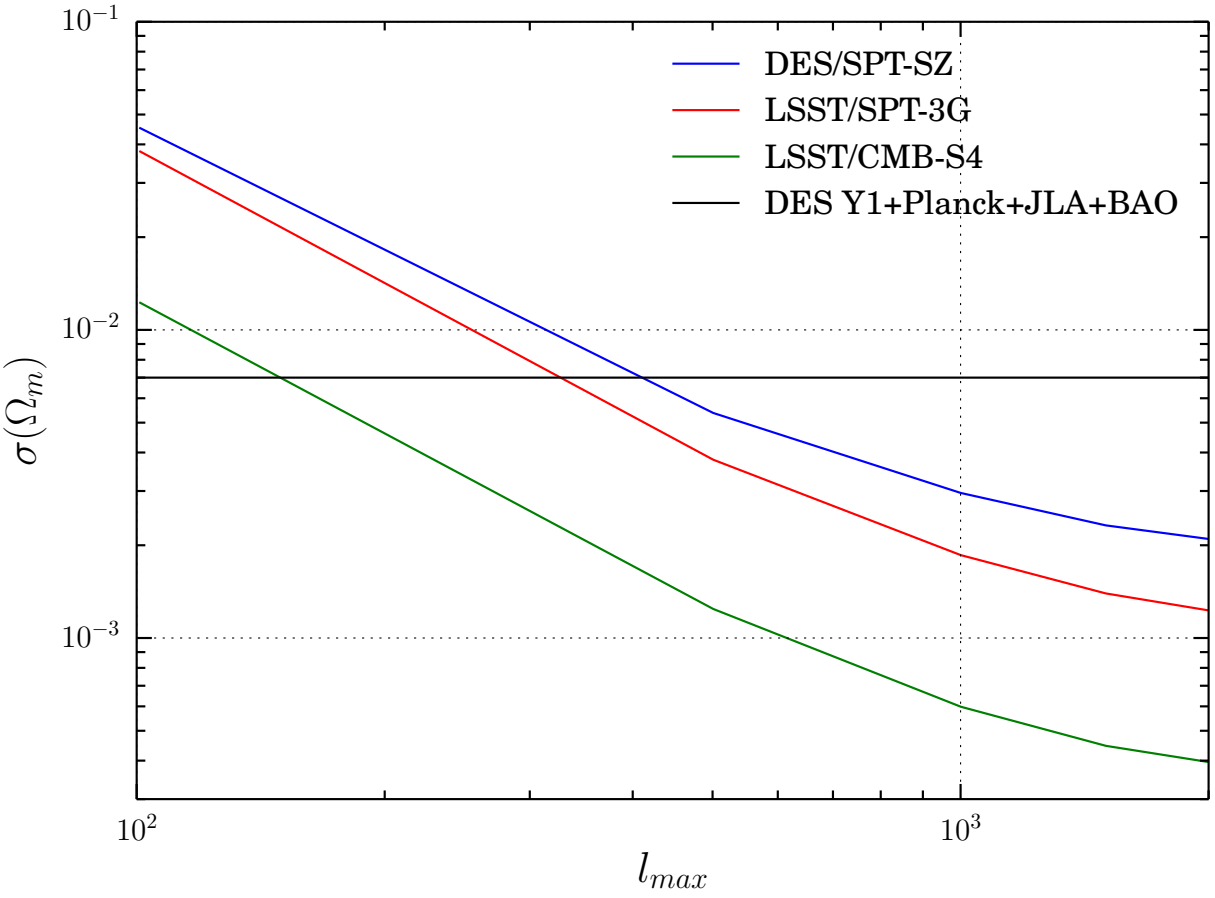

Figure 7.2: The constraints on $\Omega_{\rm m}$ for each of the survey combinations for our fiducial analysis including redshift uncertainties (same analysis as Figure 7.1). As an example of current constraints on $\Omega_{\rm m}$ from photometric surveys, we show the constraint from the recent DES year 1 analysis [16] when combined with CMB data from Planck, Type Ia supernovae data from the Joint Light-curve Analysis (JLA) and BAO data from multiple surveys (see references in [16]).

that a newer version (and perhaps older versions) of the SPT lensing map are significantly impacted by TSZ bias. This leads them to only use real space angular separations of $15'$ or greater, roughly equivalent to using an $l_{\rm max} = 720$. In [49], they use $l_{\rm max} = 1000$ for their fiducial analysis, but also vary $l_{\rm max}$ out to 2000. They cite the issues of modeling non-linear galaxy bias at small scales (large l) as a concern. On the other hand, [22] and [12] find for DES science verification galaxies that linear galaxy bias is a good approximation in most cases down to $l_{\rm max} = 2000$, even though this can be a factor of 4 smaller than where the matter power spectrum becomes non-linear.

We chose $l_{\rm max} = 1000$ for our fiducial analysis, but vary it in this section, much like the treatment in [49]. Figure 7.3 shows the σ_8 constraints for varying $l_{\rm max}$ values for the LSST/CMB-S4 measurement. We can see that $l_{\rm max}$ can significantly impact the constraints. Increasing $l_{\rm max}$ from 1000 to 2000 approximately doubles the constraining power for the $z < 1.5$ bins, though makes less of a difference in the higher redshift bins.

7.3 Dependence on $f_{\rm sky}$

Another important parameter to study is the overlapping sky fraction of the surveys $f_{\rm sky}$. We show our fiducial analysis of LSST/CMB-S4 for a range of $f_{\rm sky}$ values in Figure 7.4. On the far left of the plot, is the value $f_{\rm sky} = 0.061$, which is the overlap of DES and SPT. Keeping all other parameters the same, the increase from this overlap, to the expected overlap of $f_{\rm sky} = 0.5$ with LSST and CMB-S4 increases constraints on σ_8 by roughly a factor of three. This highlights the importance of having maximal overlap between CMB-S4, which is still in the planning phases, and LSST.

7.4 Dependence on CMB Lensing noise

In this section, we study the how the σ_8 constraints change when varying the CMB lensing noise alone. As shown in Figure 2.2, the three CMB experiments have different amounts

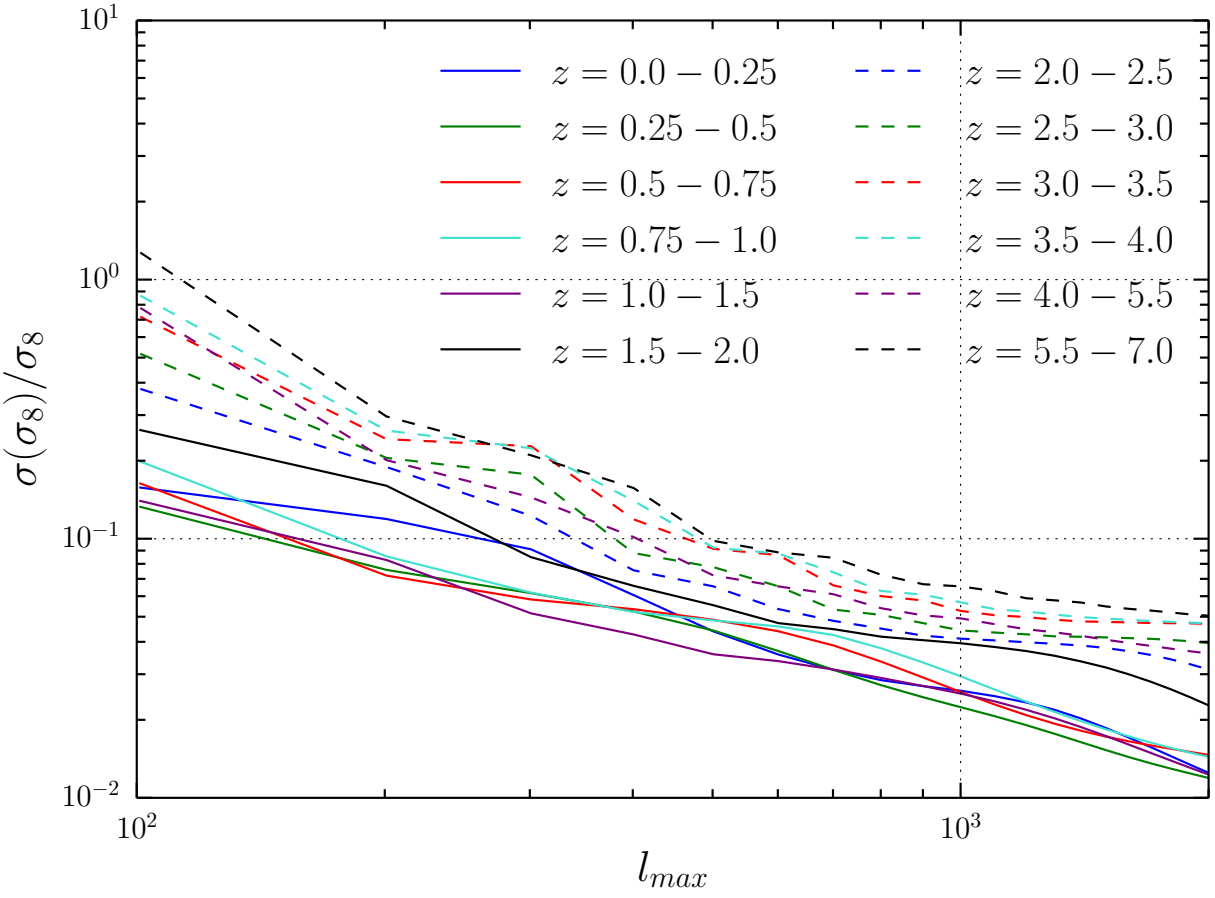

Figure 7.3: Dependence on $l_{\rm max}$ for the σ_8 constraints. We use the fiducial parameters of LSST and CMB-S4, including $f_{\rm sky} = 0.5$.

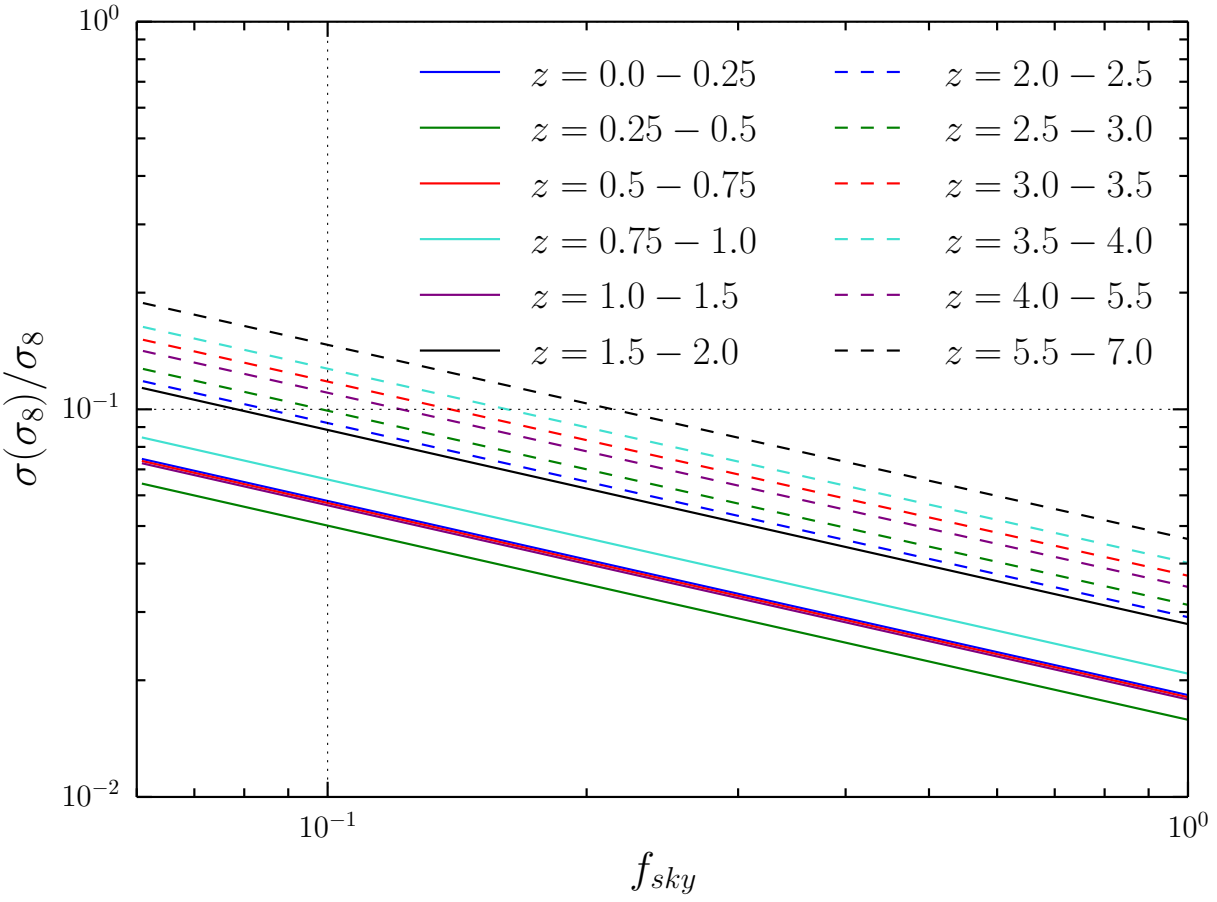

Figure 7.4: Dependence on $f_{\rm sky}$ for the σ_8 constraints. We use the fiducial parameters of LSST and CMB-S4, including $l_{\rm max} = 1000$.

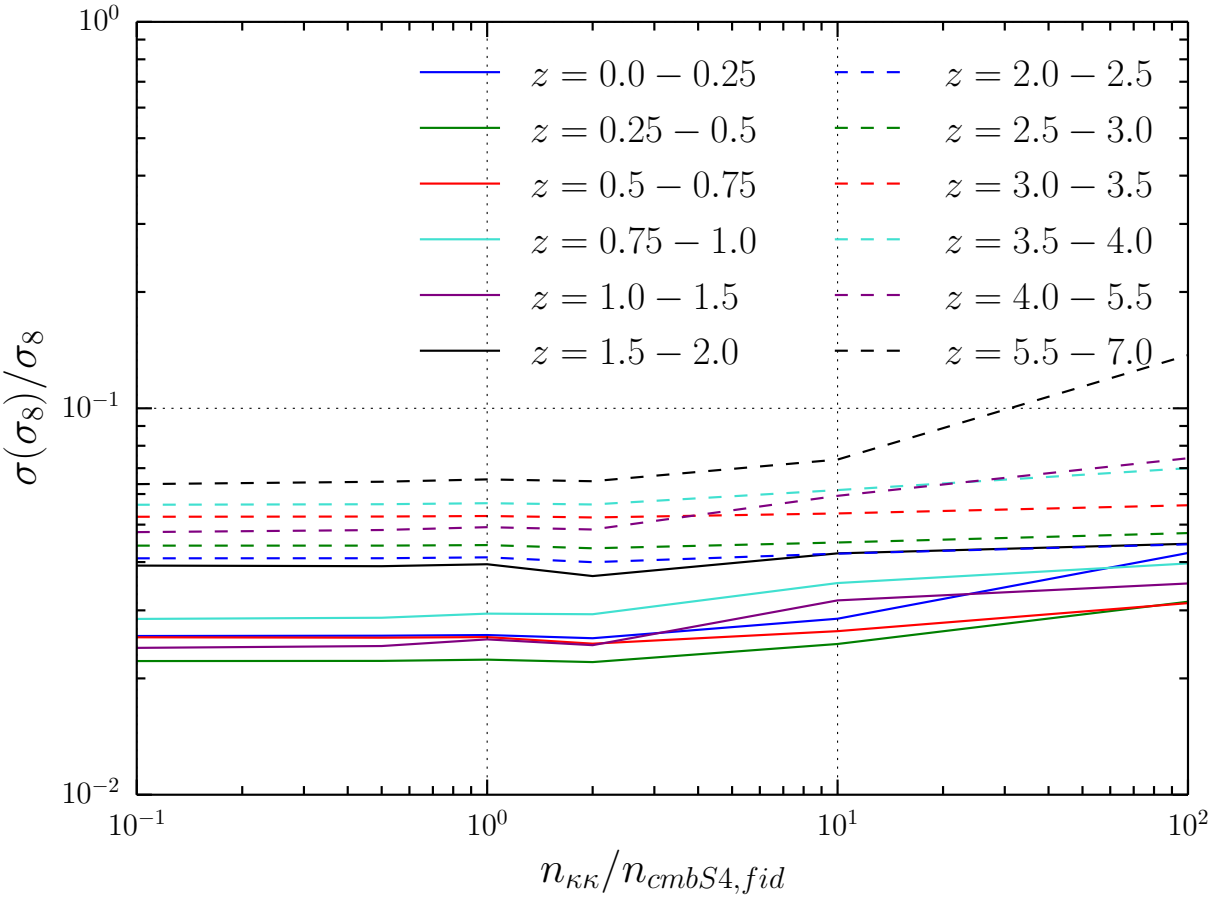

Figure 7.5: Dependence of the σ_8 constraints on CMB lensing noise in units of the fiducial prediction for CMB-S4 lensing noise. SPT-SZ is similar to a factor of about 50-100 times the lensing noise as CMB-S4. SPT-3G has about 3-8 times the noise of CMB-S4. All other parameters match the fiducial LSST+CMB-S4 analysis.

of CMB lensing noise. In Figure 7.5, we show the constraints on σ_8 for LSST/CMB-S4 when varying the CMB lensing noise. We vary the lensing noise by multiplying the fiducial CMB-S4 noise curve (Figure 2.2) by a constant factor. SPT-SZ is approximately 50-100 times more noise than CMB-S4, and SPT-3G is about 3-8 times more noise than CMB-S4 for comparison, with the factor changing with l. We see overall in Figure 7.5 that constraints only modestly depend on lensing noise, at least in the LSST era of galaxy densities. We see that increases in constraining power become less significant as the noise is decreased to lower than the fiducial CMB-S4 noise curve.

7.5 Dependence on Galaxy Density

In this section, we study how the constraints on σ_8 depend on the galaxy density. In the bins that overlap, LSST should have about 3-5 times as many galaxies as DES. Figure 7.6 shows how the fiducial LSST/CMB-S4 analysis changes when the overall galaxy density is changed. We vary the galaxy density at all redshifts by a constant factor. The figure shows only modest dependence on galaxy density. It also shows clearly that going from roughly the current era of a DES-like galaxy density to LSST produces a greater increase in precision than another factor of 3-5 would in higher galaxy density.

The results of Figures 7.5-7.6 show that in isolation, improving LSST and CMB-S4 noise only marginally improves cosmological analyses using cross-correlations of galaxies and CMB lensing. As also found in [49], these future surveys appear to be in somewhat of a sweet spot, where significant improvements could only be made by improving both the galaxy and CMB sides, and not one or the other.

7.6 Dependence on Redshift Priors

So far, our analysis has assumed no priors on any of the cosmological or redshift parameters we vary. In this section, we see how our results change when adding priors on the redshift parameters. As mentioned, photometric surveys like DES and LSST put considerable effort into calibrating photometric redshift methods, so any real analysis will have some level of prior on quantities like z_0 and σ_z. The exact priors for LSST era surveys has much uncertainty, and depends greatly on the number of available spectra at high redshifts in the future.

We apply a range of plausible priors for LSST redshifts to our analysis. A current requirement for LSST galaxy samples to be used in large-scale structure measurements, is to constrain the mean redshift of each photometric bin to $0.018(1+z)$ [36]. The target precision on redshifts in LSST is likely smaller than this for many science objectives. For example, in

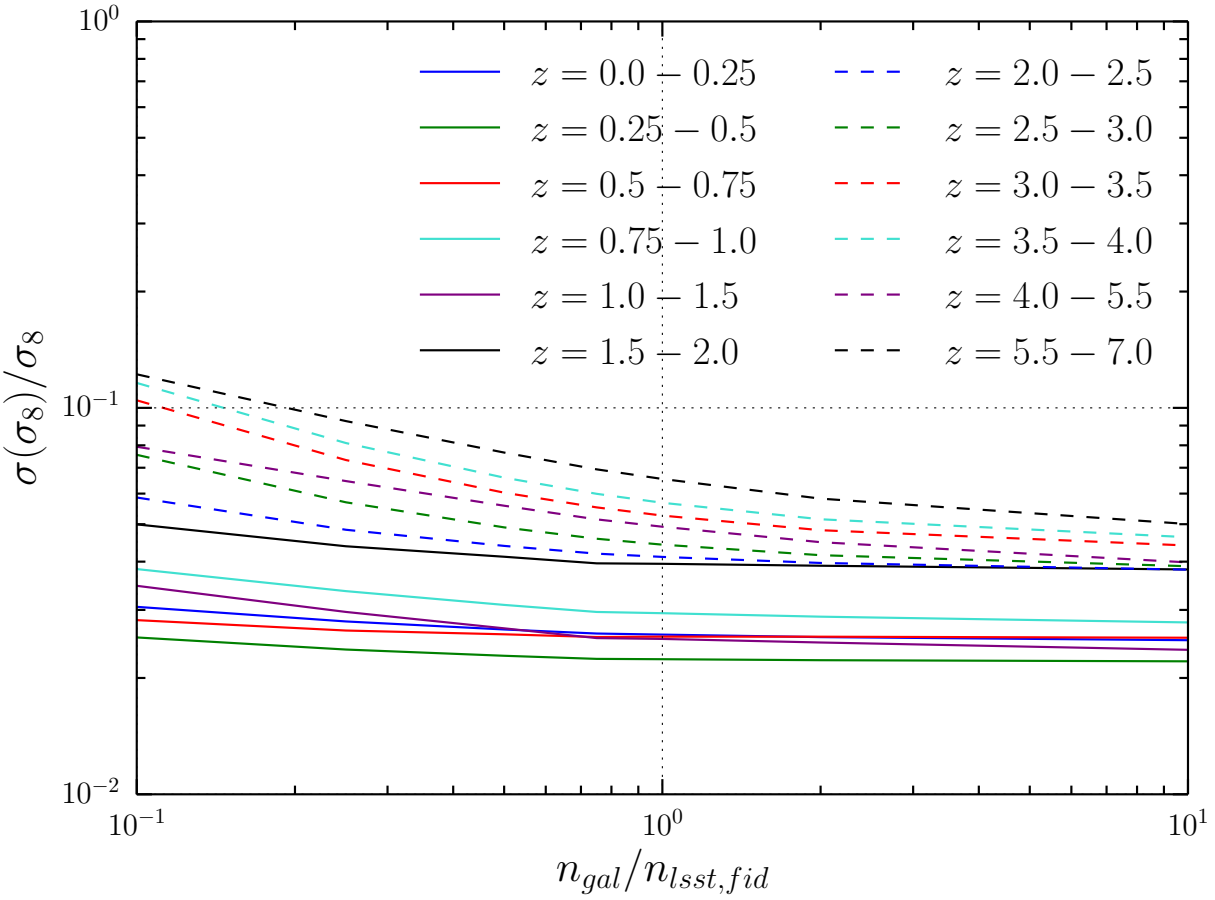

Figure 7.6: Dependence of the σ_8 constraints on galaxy density in units of fiducial LSST prediction. LSST has about 3-5 as many galaxies as DES in the bins that they overlap in. All other parameters match the fiducial LSST+CMB-S4 analysis.

[57], weak lensing constraints are projected to decrease significantly as a function of redshift uncertainty. [57] estimates a projected uncertainty on the mean redshifts of bins of $0.002(1+z)$, and finds that weak lensing cosmological constraints degrade by 30% if this uncertainty is approximately doubled, and degrade by more than 100% if the uncertainty is $0.01(1+z)$. For some redshift ranges, the priors on redshifts may be significantly better than these numbers for LSST. In [40], the spatial cross-correlation of photometric and spectroscopic galaxies could yield constraints on both the mean and width of redshift bins of $\approx 0.0004(1+z)$ for $z = 0.5 - 1.5$. The exact priors available in the LSST era will depend on a number of factors, including the number, redshift range, and magnitude depth of spectroscopic samples, the number density of the photometric samples, the types of galaxies in the photometric samples and the width of the photometrically selected bins (σ_z). Each of these factors can make constraints significantly weaker at higher redshifts. Similarly, the exact target redshift priors in the LSST era depend greatly on the different science cases and assumptions.

We use the numbers mentioned in the previous paragraph as a broad range of possible priors available in the LSST era. In Figure 7.7, we plot how the constraints on $\sigma_8(z)$ change for a range of prior assumptions on z_0 and σ_z. We plot the different scenarios for both $l_{\rm max} = 1000$ and 2000. We use the simple model of having just z_0 priors, just σ_z priors, or priors on each of the same magnitude. We make the broad assumption of having the priors scale as $(1+z)$. We can see in Figure 7.7 that the priors on σ_z are more important than the priors on z_0 for constraining σ_8. This makes sense, as σ_z and σ_8 both provide an overall scaling to the galaxy auto-correlations, which have the highest S/N of any of the power spectra. Meanwhile the dependence on z_0 is less degenerate with σ_8. (See Appendix A).

We can see in Figure 7.7 that redshift priors can improve the constraints on σ_8 considerably. For the case of priors of $0.002(1+z)$ on both z_0 and σ_z, the constraints on σ_8 improves by about a factor of 3-5 from the no priors case. When adding priors of $0.0004(1+z)$, the constraining power is within 50% of the no redshift uncertainty scenario (z_0 and σ_z fixed). This model however is almost certainly too optimistic for $z > 1.5$. We also see that the base

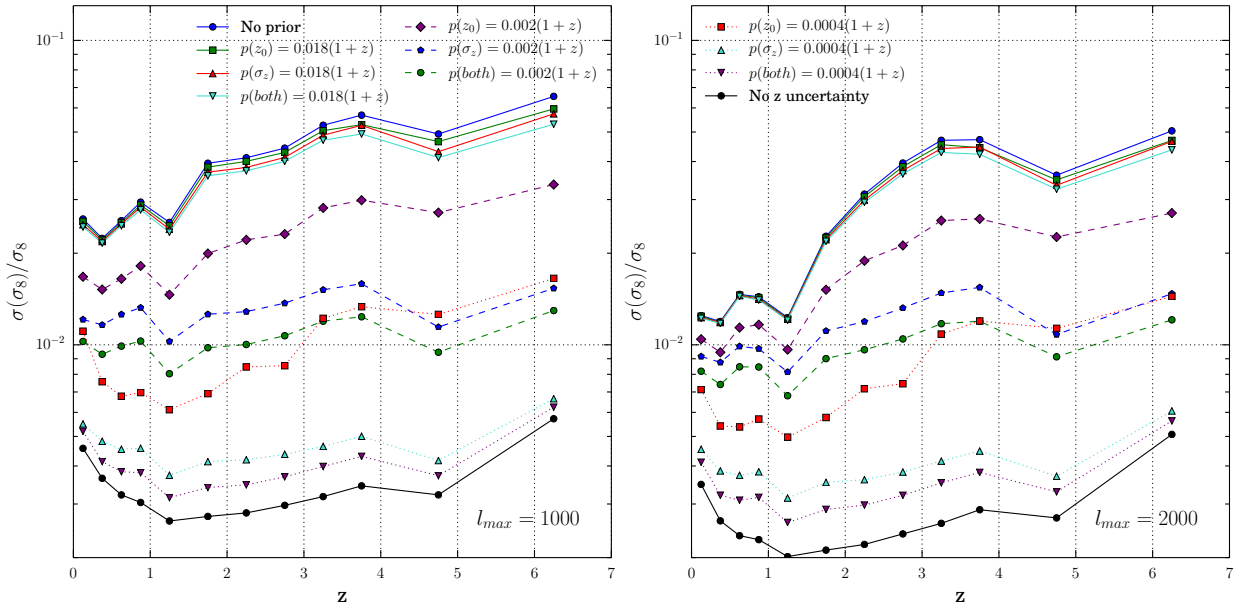

Figure 7.7: Constraints on σ_8 for our fiducial LSST/CMB-S4 analysis when adding priors on redshift parameters. Left: constraints when having $l_{\rm max} = 1000$. Right: constraints when having $l_{\rm max} = 2000$. Each curve adds either a prior on z_0, on $\sigma_{\rm z}$ or an equal prior on each. We compare the curves with priors to the fiducial case of no priors, and the opposite extreme of no redshift uncertainty with z_0 and $\sigma_{\rm z}$ fixed in the Fisher analysis.

redshift requirements for LSST large-scale structure galaxy samples, priors of $0.018(1+z)$ add very little constraining power for our fiducial analysis of LSST/CMB-S4.

In Figure 7.8, we show a similar analysis for the DES+SPT-SZ era for $l_{\rm max} = 1000$ and 2000. We project DES redshift parameter priors on the order of 0.01-0.02 based on recent calibrations of redshift bins in DES Year 1 cosmological analyses. The weak lensing source galaxies used in [16] and [55] are separated into photometrically-selected bins. The mean redshift of these bins are constrained to about an accuracy of 0.02 both in tests of photometric redshift methods on samples of spectroscopically measured galaxies [26] and in using spatial cross-correlations with spectroscopic galaxies [13]. These results were pretty constant across redshift, so we do not vary our priors with the factor $(1+z)$ here. The brighter redMaGiC galaxies used in DES year 1 results ([48], [18]) had tighter constraints on their mean redshifts from cross-correlations with spectroscopic galaxies in [11]. However,

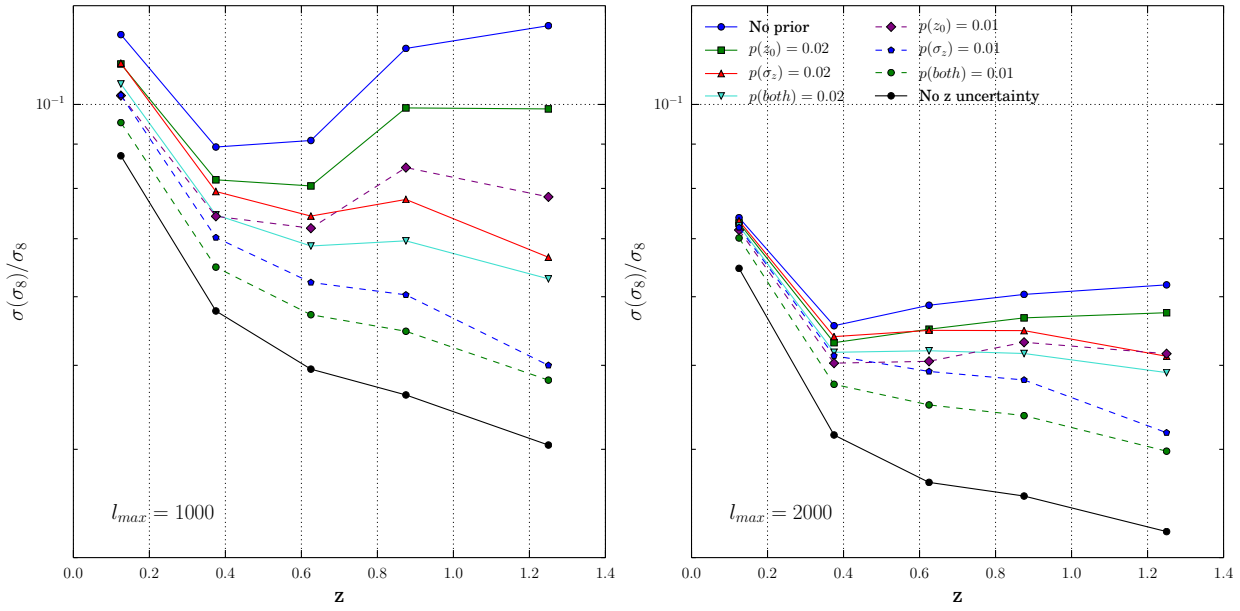

Figure 7.8: Constraints on σ_8 for the surveys DES/SPT-SZ with priors on the redshift parameters. Left: constraints with $l_{\max} = 1000$. Right: constraints with $l_{\max} = 2000$. We compare priors on z_0, σ_z and both parameters with the case of no priors, and the case of no redshift uncertainty. We base the priors on recent DES results, and do not vary them with $(1 + z)$, unlike Figure 7.7.

the modeled galaxy densities in our paper are much higher than this sample, making the weak lensing source sample a more appropriate sample to use for plausible redshift priors.

We overall see a similar dependence on redshift priors for the DES/SPT-SZ era as the future LSST/CMB-S4. Tightening the redshift priors brings results closer to the case of no redshift uncertainty. We again see that σ_z is more important than z_0 for constraining σ_8. In the DES year 1 analysis ([16] and the others mentioned above), only z_0 was constrained. Figure 7.8 (left) shows that adding a 0.02 prior on σ_z to the already achieved 0.02 prior on z_0 would improve constraints on σ_8 for the highest two redshift bins by about 30%. If $l_{\max}$ can be extended to 2000 (right side of 7.8), the gains of a 0.02 prior on σ_z only go up to 15%.

CHAPTER 8

CONSTRAINTS ON REDSHIFT PARAMETERS

We focus briefly again in this section on the ability of galaxy clustering and galaxy-CMB lensing correlation measurements to 'self-calibrate' redshifts and compare those constraints to photometric redshift techniques. The idea of calibrating redshifts strictly from correlation functions was studied in more detail recently in [27]. A significant difference in this work though is not fixing the cosmology while solving for redshift parameters.

As mentioned in Chapter 7.6, the Dark Energy Survey is already calibrating the mean redshift of bins to an uncertainty of about 0.02. The Large Synoptic Survey Telescope broadly has a requirement of constraining the mean of redshift bins to $0.018(1+z)$, though likely that number can easily be beaten at low redshift. As mentioned in Chapter 7.6, various analyses predict far stronger constraints in the LSST era, and certain scientific applications will require better than this $0.018(1+z)$ target. In Figure 8.1, we compare these broad baselines for redshift constraints to our Fisher constraints on σ_z and z_0 with no priors applied. We call $0.002(1+z)$ a "goal" of LSST ([57], [40]), though really a suitable goal varies depending on the science measurement and the precision desired. This number is not necessarily a universal goal. We show results for both $l_{\rm max} = 1000$ and 2000 in Figure 8.1. The projections on DES from correlations with SPT beat the current threshold of 0.02 constraints on the redshift parameters in the first three redshift bins, even if only $l_{\rm max} = 1000$ can be used. As mentioned previously, currently DES has only constrained the mean redshift of bins, z_0 and not the width, σ_z. Work in e.g. [39] suggests constraints on each parameter should be comparable though from spatial cross-correlations with spectroscopic galaxies. For LSST, the constraints for $l_{\rm max} = 2000$ at low redshifts ($z < 1.5$) are stronger than the goal $0.002(1+z)$ uncertainty on z_0 and σ_z. For $l_{\rm max} = 1000$, the constraints are weaker than this goal, though still within a factor of 2 at $z < 1$. The constraints from the power spectra for most redshift bins, and both $l_{\rm max}$ values are better than the LSST requirement ([36]) of $0.018(1+z)$ for large-scale structure analyses. Even if the constraints of 'self-calibrating'

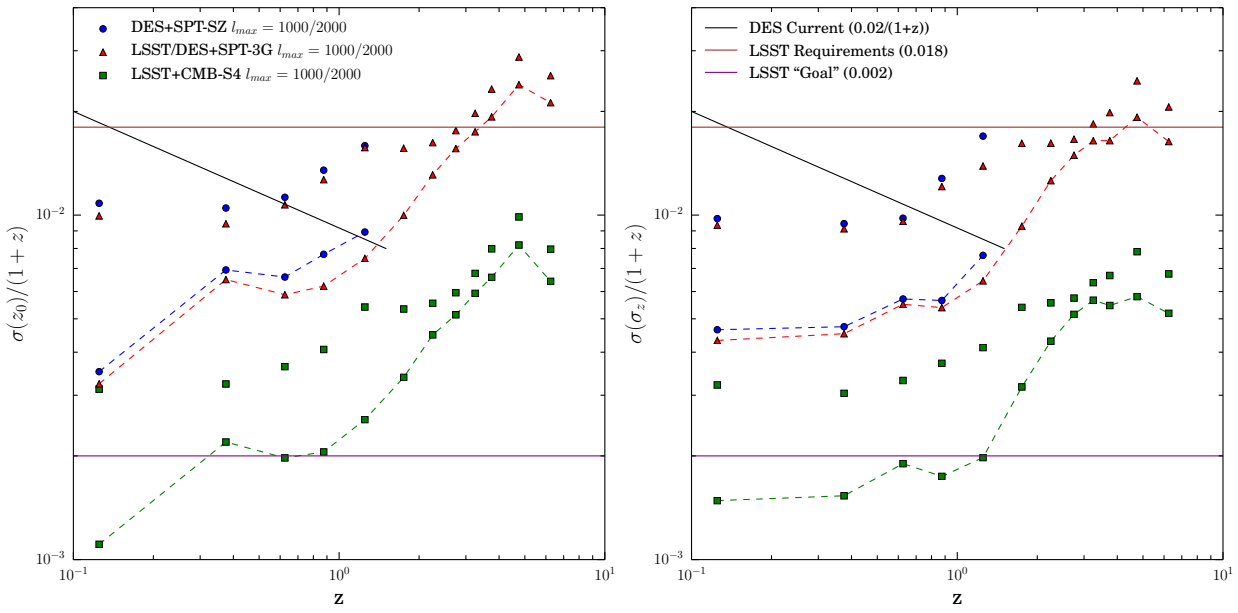

Figure 8.1: The constraints on the mean of a binned redshift distribution (left) and the width of the distribution (right) for our fiducial analyses of different surveys. The unconnected points are with $l_{\rm max} = 1000$ and the dotted lines are with $l_{\rm max} = 2000$. We compare these constraints to the current approximate DES constraints for mean redshifts in a bin from photometric redshift methods [13], and some target constraints for both redshift parameters in LSST. The LSST requirements are from [36]. The LSST "goal" is from [57] and mentioned in [40], though we note that redshift goals in LSST vary for different measurements, and this value is not a universal target. We also note that DES has not tried to constrain $\sigma_{\rm z}$ directly in data, so we show its constraints on z_0 in both plots. These constraints from DES are roughly constant with redshift, so we see a decrease with redshift when plotting $\sigma_{\rm z}(1+z)$.

redshifts from power spectra measurements are merely comparable to traditional methods of photometric redshift estimation, this could add significant information to cosmic surveys. A discrepancy could point to systematics in either the photometric redshift or power spectra measurements.

CHAPTER 9

CONCLUSIONS

In this work, we sought to answer two questions: 1. How are analyses of galaxy clustering and CMB lensing affected by uncertainties in redshift parameters and 2. Can redshift parameters be self-calibrated by galaxy and CMB lensing correlations. We found in Chapter 6 that the presence of redshift uncertainties can increase errors on e.g. $\sigma_8(z)$ by an order of magnitude. We showed the importance of using the cross-correlations of different galaxy bins ($C_l^{g_i g_j}$), which in the assumption of perfect redshift knowledge is not a necessary measurement.

Though the redshift uncertainties degrades the analysis, the projected cosmological constraints are still fairly impressive. Our fiducial analysis (Figure 7.1) constrains σ_8 in each redshift bin in the DES/SPT-SZ era to about 10%. For LSST/CMB-S4, the constraints get down to $2-3\%$ at low redshifts ($z < 1.5$), and only a few % higher at higher redshifts. Constraints of this level should help in distinguishing between ΛCDM and models of modified general relativity as the cause of cosmic acceleration. As a comparison, [37] predicts 2% measurements on $\sigma_8(z)$ from $z = 0.5 - 3$ from LSST weak lensing and BAO data plus Planck CMB results, and finds that these constraints could decisively rule out e.g. a DGP modified GR model [17].

In Chapter 7, we explored what survey parameters most affect these measurements of cosmological and redshift parameters. Among different survey parameters explored individually, we found the largest dependences on: $f_{\rm sky}$, $l_{\rm max}$ and priors on the redshift parameters. The constraining power can be doubled or better by increasing $l_{\rm max}$ from 1000 to 2000 (Figure 7.3) or with good priors on the redshift parameters from other data sources (e.g. Figure 7.7). The analysis of $f_{\rm sky}$ (Figure 7.4) shows that the significant increase in overlap of surveys in the future (LSST/CMB-S4 will have 8 times as much overlapping area as DES/SPT), accounts for much of the increased precision on σ_8. In contrast, we found that increasing the galaxy density (Figure 7.6) or reducing the CMB lensing noise (Figure 7.5) beyond expectations for LSST/CMB-S4 only marginally improve constraints. As also found in [49],

the improvements of LSST and CMB-S4 in terms of galaxy density and CMB lensing noise seem to work together, such that improving either individually further has minimal gain.

We also showed in Chapter 8 the constraints on redshift parameters from the Fisher analysis and compared them to current and expected constraints on redshift parameters from photometric redshift techniques (Figure 8.1). The constraints projected in this work are comparable to the photometric techniques. This suggests that 'self-calibration' of redshift parameters from cosmological measurements themselves can be competitive with other techniques. That such constraints can be achieved simultaneously with cosmological constraints (i.e. σ_8) is an important finding for the feasibility of this method as a redshift probe.

A number of assumptions were made in this work that may need more study in the future. The largest element that was a focus of this work was the redshift distribution modeling. A two-parameter Gaussian model may not be sufficient for accurately incorporating redshift distributions and their uncertainties into analyses on data. More work on the resilience of this model, and extensions to make the model more flexible should be done. An advantage of the simple model we use is the strong dependence of the power spectra on the redshift parameters. This allows for 'self-calibration' of redshift parameters from just the power spectra measurements. A risk in having too many redshift parameters is creating degeneracies where multiple redshift parameters may impact the power spectra in similar ways.

There are several other possibly impactful parameters not addressed in this work which are mentioned in [49], whose analysis we broadly followed in order to isolate the effects of adding redshift uncertainty. These factors include non-linear galaxy bias, non-Gaussian terms in the covariance, redshift space distortions, biases in the CMB lensing map, and differences between a Monte Carlo analysis and a Fisher analysis. [49] also note that bispectra could add useful information to an analysis like this.

This work should highlight the importance of incorporating redshift uncertainty and modeling into cosmological analyses using galaxies and CMB lensing, as well as inspire more work on 'self-calibrating' redshifts with these and other measurements. While we did

not use weak gravitational lensing of galaxies, similar concerns about redshift uncertainties and modeling should be studied for using that probe, and many of the techniques in this work could be applied. The issue of how to address redshift uncertainty has never been more important than the upcoming era of LSST, where we will be probing redshift regimes currently still sparse in available spectroscopic measurements for calibrating photometric redshift techniques.

REFERENCES

[1] K. N. Abazajian, P. Adshead, and Z. Ahmed, et al. CMB-S4 Science Book, First Edition. *ArXiv e-prints*, October 2016.

[2] K. N. Abazajian, K. Arnold, and J. Austermann, et al. Neutrino physics from the cosmic microwave background and large scale structure. *Astroparticle Physics*, 63:66–80, March 2015.

[3] T. M. C. Abbott, F. B. Abdalla, S. Allam, and A. Amara, et al. The Dark Energy Survey Data Release 1. *ArXiv e-prints*, January 2018.

[4] J. E. Austermann, K. A. Aird, and J. A. Beall. SPTpol: an instrument for CMB polarization measurements with the South Pole Telescope. In *Millimeter, Submillimeter, and Far-Infrared Detectors and Instrumentation for Astronomy VI*, volume 8452, page 84521E, September 2012.

[5] E. Baxter, J. Clampitt, and T. Giannantonio, et al. Joint measurement of lensing-galaxy correlations using SPT and DES SV data. *MNRAS*, 461:4099–4114, October 2016.

[6] E. J. Baxter, Y. Omori, and C. Chang, et al. Dark Energy Survey Year 1 Results: Methodology and Projections for Joint Analysis of Galaxy Clustering, Galaxy Lensing, and CMB Lensing Two-point Functions. *ArXiv e-prints*, February 2018.

[7] B. A. Benson, P. A. R. Ade, and Z. Ahmed, et al. SPT-3G: a next-generation cosmic microwave background polarization experiment on the South Pole telescope. In *Millimeter, Submillimeter, and Far-Infrared Detectors and Instrumentation for Astronomy VII*, volume 9153, page 91531P, July 2014.

[8] L. E. Bleem, A. van Engelen, and G. P. Holder, et al. A Measurement of the Correlation of Galaxy Surveys with CMB Lensing Convergence Maps from the South Pole Telescope. *ApJl*, 753:L9, July 2012.

[9] C. Bonnett, M. A. Troxel, and W. Hartley. Redshift distributions of galaxies in the Dark Energy Survey Science Verification shear catalogue and implications for weak lensing. *Phys. Rev. D*, 94(4):042005, August 2016.

[10] J. E. Carlstrom, P. A. R. Ade, and K. A. Aird, et al. The 10 Meter South Pole Telescope. *PASP*, 123:568, May 2011.

[11] R. Cawthon, C. Davis, M. Gatti, and P. Vielzeuf, et al. Dark Energy Survey Year 1 Results: Calibration of redMaGiC Redshift Distributions in DES and SDSS from Cross-Correlations. *ArXiv e-prints*, December 2017.

[12] M. Crocce, J. Carretero, and A. H. Bauer, et al. Galaxy clustering, photometric redshifts and diagnosis of systematics in the DES Science Verification data. *MNRAS*, 455:4301–4324, February 2016.

[13] C. Davis, M. Gatti, P. Vielzeuf, and R. Cawthon, et al. Dark Energy Survey Year 1 Results: Cross-Correlation Redshifts in the DES – Calibration of the Weak Lensing Source Redshift Distributions. *ArXiv e-prints*, October 2017.

[14] K. S. Dawson, D. J. Schlegel, and C. P. Ahn, et al. The Baryon Oscillation Spectroscopic Survey of SDSS-III. *AJ*, 145:10, January 2013.

[15] J. T. A. de Jong, K. Kuijken, and D. Applegate, et al. The Kilo-Degree Survey. *The Messenger*, 154:44–46, December 2013.

[16] DES Collaboration, et al. Dark Energy Survey Year 1 Results: Cosmological Constraints from Galaxy Clustering and Weak Lensing. *ArXiv e-prints*, August 2017.

[17] G. Dvali, G. Gabadadze, and M. Porrati. 4D gravity on a brane in 5D Minkowski space. *Physics Letters B*, 485:208–214, July 2000.

[18] J. Elvin-Poole, M. Crocce, and A. J. Ross, et al. Dark Energy Survey Year 1 Results: Galaxy clustering for combined probes. *ArXiv e-prints*, August 2017.

[19] B. Flaugher. The Dark Energy Survey. *International Journal of Modern Physics A*, 20:3121–3123, 2005.

[20] A. Font-Ribera, P. McDonald, and N. Mostek, et al. DESI and other Dark Energy experiments in the era of neutrino mass measurements. *J. Cosmology Astropart. Phys.*, 5:023, May 2014.

[21] M. Gatti, P. Vielzeuf, C. Davis, and R. Cawthon, et al. Dark Energy Survey Year 1 results: cross-correlation redshifts - methods and systematics characterization. *MNRAS*, 477:1664–1682, June 2018.

[22] T. Giannantonio, P. Fosalba, and R. Cawthon, et al. CMB lensing tomography with the DES Science Verification galaxies. *MNRAS*, 456:3213–3244, March 2016.

[23] A. Gorecki, A. Abate, and R. Ansari, et al. A new method to improve photometric redshift reconstruction. Applications to the Large Synoptic Survey Telescope. *Astronomy and Astrophysics*, 561:A128, January 2014.

[24] C. Heymans, L. Van Waerbeke, and L. Miller, et al. CFHTLenS: the Canada-France-Hawaii Telescope Lensing Survey. *MNRAS*, 427:146–166, November 2012.

[25] C. Howlett, A. Lewis, A. Hall, and A. Challinor. CMB power spectrum parameter degeneracies in the era of precision cosmology. *J. Cosmology Astropart. Phys.*, 4:027, April 2012.

[26] B. Hoyle, D. Gruen, and G. M. Bernstein, et al. Dark Energy Survey Year 1 Results: redshift distributions of the weak-lensing source galaxies. *MNRAS*, 478:592–610, July 2018.

[27] B. Hoyle and M. M. Rau. Self-consistent redshift estimation using correlation functions without a spectroscopic reference sample. *ArXiv e-prints*, February 2018.

[28] D. Huterer, D. Kirkby, and R. Bean, et al. Growth of cosmic structure: Probing dark energy beyond expansion. *Astroparticle Physics*, 63:23–41, March 2015.

[29] Ž. Ivezić, S. M. Kahn, and J. Tyson, et al. LSST: from Science Drivers to Reference Design and Anticipated Data Products. *ArXiv e-prints*, May 2008.

[30] N. Kaiser. Weak gravitational lensing of distant galaxies. *ApJ*, 388:272–286, April 1992.

[31] D. Kirk, Y. Omori, A. Benoit-Lévy, and R. Cawthon, et al. Cross-correlation of gravitational lensing from DES Science Verification data with SPT and Planck lensing. *MNRAS*, 459:21–34, June 2016.

[32] M. Levi, C. Bebek, and T. Beers, et al. The DESI Experiment, a whitepaper for Snowmass 2013. *ArXiv e-prints*, August 2013.

[33] A. Lewis, A. Challinor, and A. Lasenby. Efficient Computation of Cosmic Microwave Background Anisotropies in Closed Friedmann-Robertson-Walker Models. *ApJ*, 538:473–476, August 2000.

[34] D. N. Limber. The Analysis of Counts of the Extragalactic Nebulae in Terms of a Fluctuating Density Field. *ApJ*, 117:134, January 1953.

[35] LSST Dark Energy Science Collaboration. Large Synoptic Survey Telescope: Dark Energy Science Collaboration. *ArXiv e-prints*, November 2012.

[36] LSST Dark Energy Science Collaboration. Lsst dark energy science collaboration science requirements document. *in prep.*, 2018.

[37] LSST Science Collaboration, et al. LSST Science Book, Version 2.0. *ArXiv e-prints*, December 2009.

[38] S. Miyazaki, Y. Komiyama, and H. Nakaya, et al. Hyper Suprime-Cam. In *Ground-based and Airborne Instrumentation for Astronomy IV*, volume 8446, page 84460Z, September 2012.

[39] J. A. Newman. Calibrating Redshift Distributions beyond Spectroscopic Limits with Cross-Correlations. *ApJ*, 684:88–101, September 2008.

[40] J. A. Newman, A. Abate, and F. B. Abdalla, et al. Spectroscopic needs for imaging dark energy experiments. *Astroparticle Physics*, 63:81–100, March 2015.

[41] T. Okamoto and W. Hu. Cosmic microwave background lensing reconstruction on the full sky. *Phys. Rev. D*, 67(8):083002, April 2003.

[42] Y. Omori, R. Chown, and G. Simard, et al. A 2500 deg^2 CMB Lensing Map from Combined South Pole Telescope and Planck Data. *ApJ*, 849:124, November 2017.

[43] Y. Omori and G. Holder. Cross-Correlation of CFHTLenS Galaxy Number Density and Planck CMB Lensing. *ArXiv e-prints*, February 2015.

[44] Y. Ono, M. Ouchi, and Y. Harikane, et al. Great Optically Luminous Dropout Research Using Subaru HSC (GOLDRUSH). I. UV luminosity functions at z 4-7 derived with the half-million dropouts on the 100 deg^2 sky. *PASJ*, 70:S10, January 2018.

[45] Planck Collaboration, et al. Planck 2015 results. XIII. Cosmological parameters. *ArXiv e-prints*, February 2015.

[46] Planck Collaboration, et al. Planck 2015 results. VIII. High Frequency Instrument data processing: Calibration and maps. *Astronomy and Astrophysics*, 594:A8, September 2016.

[47] J. Prat, C. Sánchez, and Y. Fang, et al. Dark Energy Survey Year 1 Results: Galaxy-Galaxy Lensing. *ArXiv e-prints*, August 2017.

[48] E. Rozo, E. S. Rykoff, and A. Abate, et al. redMaGiC: selecting luminous red galaxies from the DES Science Verification data. *MNRAS*, 461:1431–1450, September 2016.

[49] M. Schmittfull and U. Seljak. Parameter constraints from cross-correlation of CMB lensing with galaxy clustering. *ArXiv e-prints*, October 2017.

[50] K. M. Smith, O. Zahn, and O. Doré. Detection of gravitational lensing in the cosmic microwave background. *Phys. Rev. D*, 76(4):043510, August 2007.

[51] R. E. Smith, J. A. Peacock, and A. Jenkins, et al. Stable clustering, the halo model and non-linear cosmological power spectra. *MNRAS*, 341:1311–1332, June 2003.

[52] C. C. Steidel and D. Hamilton. Deep imaging of high redshift QSO fields below the Lyman limit. I - The field of Q0000-263 and galaxies at Z = 3.4. *AJ*, 104:941–949, September 1992.

[53] K. T. Story, C. L. Reichardt, and Z. Hou, et al. A Measurement of the Cosmic Microwave Background Damping Tail from the 2500-Square-Degree SPT-SZ Survey. *ApJ*, 779:86, December 2013.

[54] The Planck Collaboration. The Scientific Programme of Planck. *ArXiv Astrophysics e-prints*, April 2006.

[55] M. A. Troxel, N. MacCrann, and J. Zuntz, et al. Dark Energy Survey Year 1 Results: Cosmological Constraints from Cosmic Shear. *ArXiv e-prints*, August 2017.

[56] A. van Engelen, R. Keisler, and O. Zahn, et al. A Measurement of Gravitational Lensing of the Microwave Background Using South Pole Telescope Data. *ApJ*, 756:142, September 2012.

[57] H. Zhan. Cosmic tomographies: baryon acoustic oscillations and weak lensing. *J. Cosmology Astropart. Phys.*, 8:008, August 2006.

APPENDIX A

POWER SPECTRA DEPENDENCE ON PARAMETERS

To get a better intuition of which power spectra constrain which parameters, Figure A.1 shows $dC_l/d\theta$ for the various combinations of spectra and parameters for the redshift bins $0.75 < z_{\rm ph} < 1.0$ with $z_0 = 0.871$ and $\sigma_{\rm z} = 0.117$ and the redshift bin $2.0 < z_{\rm ph} < 2.5$ with $z_0 = 2.178$ and $\sigma_{\rm z} = 0.216$. We show two redshift bins to broadly see trends of how dependence on different parameters changes with redshift.

We can see for the galaxy auto-power spectra (top row), which are also the highest S/N spectra, the parameters $b_{\rm g}$ and σ_8 equivalently scale the spectra. We also see that increasing $b_{\rm g}$ and $\sigma_{\rm z}$ both directly scale the galaxy auto-power spectra at all scales (in our modeling of no scale-dependent galaxy bias). Other than a normalization factor of the step sizes in the plot, for the galaxy auto-spectra, $b_{\rm g}$, σ_8 and $\sigma_{\rm z}$ are degenerate. Adding the galaxy-CMB lensing cross-spectra (middle row), can break the degeneracy of $b_{\rm g}$ and σ_8, but has little dependence on $\sigma_{\rm z}$. The cross-spectra of adjacent galaxy redshift bins (bottom row) have a large dependence on $\sigma_{\rm z}$, in a way that is not degenerate with other parameters. These plots show that both the galaxy-CMB lensing cross-spectra, and galaxy-galaxy cross-spectra are necessary to break the degeneracy between $b_{\rm g}$, σ_8 and $\sigma_{\rm z}$ that arises when incorporating redshift uncertainties.

We can also see that the parameters z_0 and $\Omega_{\rm m}$ are largely not degenerate with other parameters in the galaxy auto-spectra (top row). For this reason, constraints on these parameters are less correlated with e.g. σ_8 improvements (Figure 6.2).

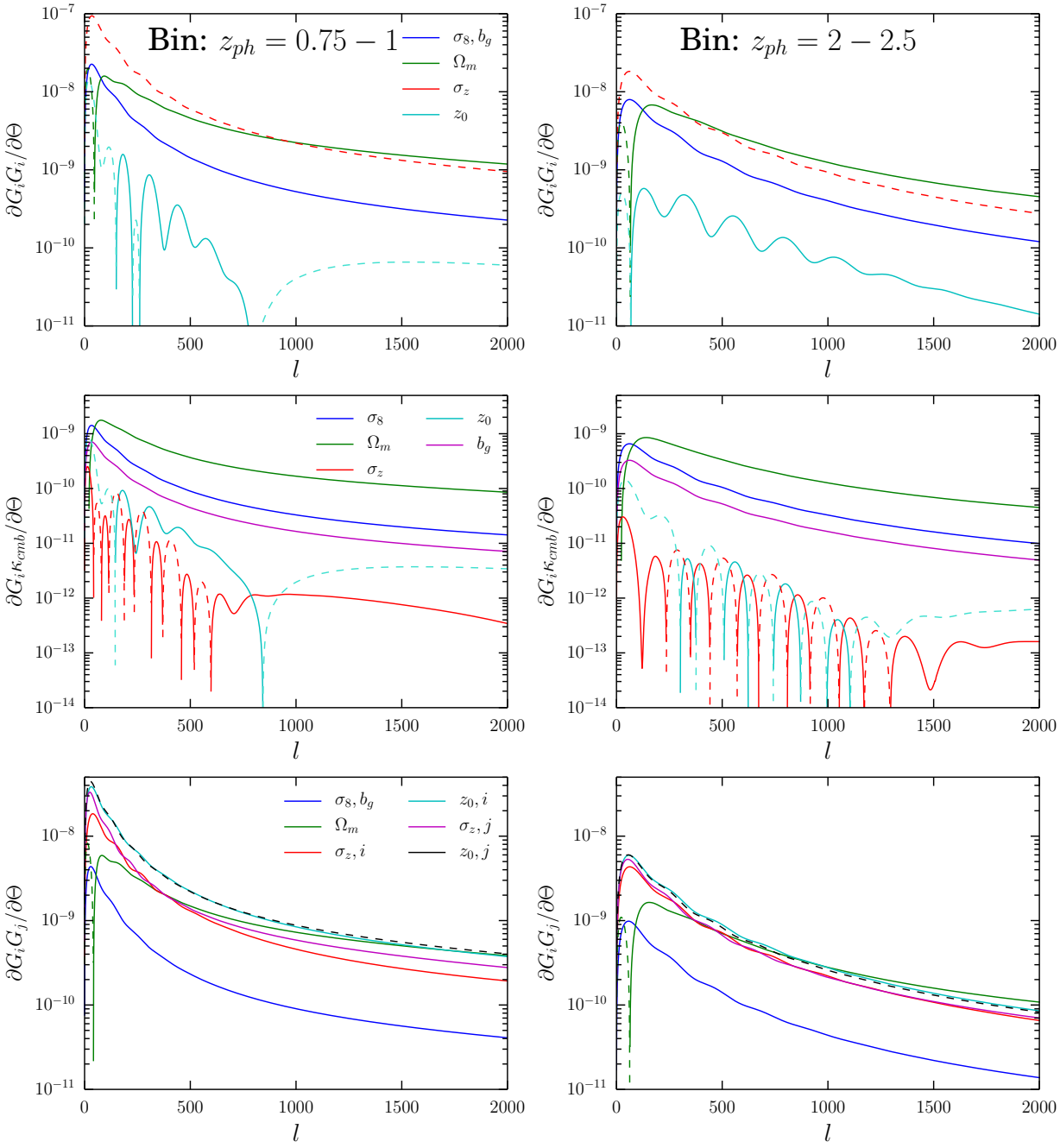

Figure A.1: Parameter dependence for the galaxy auto-power spectra (top), galaxy-CMB lensing cross spectra (middle row) and the cross spectra of two adjacent galaxy bins (bottom row). Shown are the spectra for the redshift bin $0.75 < z_{\rm ph} < 1.0$ (left) and $2.0 < z_{\rm ph} < 2.5$ (right). Dotted lines signify a negative correlation with the parameter and the spectra. For the galaxy cross spectra, the listed bins are the jth bin, and are cross-correlated with their neighboring lower redshift bins ($0.5 < z < 0.75$ and $1.5 < z < 2.0$ respectively) which are the ith bins in the bottom row.